Torabi, Jalal; Niiranen, Jarkko; Ansari, Reza

Nonlinear finite element analysis within strain gradient elasticity: Reissner-Mindlin plate theory versus three-dimensional theory

Published in:
European Journal of Mechanics A: Solids

DOI:
10.1016/j.euromechsol.2021.104221

Published: 01/05/2021

Document Version
Publisher's PDF, also known as Version of record

European Journal of Mechanics / A Solids 87 (2021) 104221

Contents lists available at ScienceDirect

European Journal of Mechanics / A Solids

journal homepage: http://www.elsevier.com/locate/ejmsol

Nonlinear finite element analysis within strain gradient elasticity: Reissner-Mindlin plate theory versus three-dimensional theory

Jalal Torabi [a,b,*], Jarkko Niiranen [a], Reza Ansari [b]

[a] Department of Civil Engineering, School of Engineering, Aalto University, P.O. Box 12100, Aalto, 00076, Finland
[b] Faculty of Mechanical Engineering, University of Guilan, P.O. Box 3756, Rasht, Iran

ARTICLE INFO

Keywords:
Finite element method
Strain gradient theory
Nonlinear bending analysis
Plates
3D elasticity
First-order shear deformation theory

ABSTRACT

Nonlinear plate bending within Mindlin's strain gradient elasticity theory (SGT) is investigated by employing somewhat non-standard finite element methods. The main goal is to compare the bending results provided by the geometrically nonlinear three-dimensional (3D) theory and the geometrically nonlinear Reissner–Mindlin plate theory, i.e., the first-order shear deformation plate theory (FSDT), within the SGT. For the 3D theory, the nonlinear Green–Lagrange strain relations are adopted, while the von Kármán nonlinear strains are employed for the FSDT. The matrix-vector forms of the energy functionals are derived for both models. In order to perform the corresponding finite element discretizations, a quasi-C^1-continuous 4-node tetrahedral solid element and a quasi-C^1-continuous 6-node triangular plate element are employed for the 3D model and plate model, respectively. The first-order derivatives of the primal problem quantities are employed as additional nodal values to respond to the continuity requirements of class C^1. A variety of computational results highlighting the differences between the 3D and FSDT models are given for two different plate geometries: a rectangular plate with a circular hole and an elliptical plate.

1. Introduction

A wide range of non-classical continuum models such as nonlocal theories (Eringen, 1972, 1983bib_Eringen_1972bib_Eringen_1983; Ansari and Torabi, 2016; Barretta et al., 2019; Romano and Barretta, 2017), couple stress theory (Mindlin and Tiersten, 1962; Park and Gao, 2006) and strain gradient theory (SGT) (Mindlin, 1964, 1965bib_Mindlin_1964bib_Mindlin_1965) have been comprehensively utilized in order to analyze the structural behavior of micro/nanostructures or microarchitectural structures (Khakalo et al., 2018; Khakalo and Niiranen, 2020; Khakalo and Niiranen, 2019; Khakalo and Niiranen, 2018; dell'Isola et al., 2019; Dell'Isola et al., 2019a). Mindlin's SGT (Mindlin, 1964) poses a size-dependent continuum theory with five non-classical length scale parameters, in the case of isotropic materials, providing an infrastructure to account for size-effects. The modified SGT was later proposed by Lim et al. (Lam et al., 2003) and extensions for different beam (Lazopoulos and Lazopoulos, 2010; Wang et al., 2010, 2011bib_Wang_et_al_2010; Ghayesh et al., 2013; Kahrobaiyan et al., 2011bib_Wang_et_al_2011; Zhang and Gao, 2020), plate (Lestringant and Audoly, 2020; Ramezani, 2012; Movassagh and Mahmoodi, 2013; Thai and Choi, 2013; Ansari et al., 2015a; Nguyen et al., 2019) and shell (Lazopoulos and Lazopoulos, 2011; Zeighampour et al., 2018; Zhang et al., 2015; Balobanov et al., 2019; Mirjavadi et al., 2019) models were presented in different works by different authors. Both geometrically linear and nonlinear analyses have been considered. For instance, Wang et al. (2010) proposed a micro-scale Timoshenko beam model following the SGT. A nonlinear SGT Euler–Bernoulli beam model was derived by Kahrobaiyan et al. (2011). Recently, Zhang and Gao (2020) proposed a reformulated SGT for the Euler–Bernoulli beam model, although the model takes the same generic form as the earlier corresponding beams models compared in (Hosseini et al., 2019). The asymptotically exact strain-gradient models for nonlinear slender elastic structures were also presented by Lestringant and Audoly (2020) in which the governing equation of the 1D strain gradient model for a hyper-elastic cylinder was derived. Ramezani (2012) introduced a shear deformation microplate formulation under the SGT and analytically studied some linear static and dynamic problems. Furthermore, Ansari et al. (2015a) comprehensively studied vibration, bending and buckling of functionally graded (FG) circular/annular microplates according to the modified strain gradient theory (MSGT) and an axisymmetric formulation of the

* Corresponding author. Department of Civil Engineering, School of Engineering, Aalto University, P.O. Box 12100, Aalto, 00076, Finland.
E-mail address: jalal.torabi@aalto.fi (J. Torabi).

https://doi.org/10.1016/j.euromechsol.2021.104221
Received 14 July 2020; Received in revised form 30 November 2020; Accepted 11 January 2021
Available online 19 January 2021
0997-7538/

FSDT. The strain gradient vibration analysis of cracked microplates was also highlighted by Nguyen et al. (2019) using the extended IGA. In the case of shells, Lazopoulos et al. (Lazopoulos and Lazopoulos, 2011) proposed a nonlinear thin shallow shell model by a simple version of the SGT. A shear deformation model for FG cylindrical microshells based on the SGT was also presented by Zhang et al. (2015). A general Kirchhoff–Love shell formulation of the SGT, with a conforming finite element formulation and benchmarks, was introduced by Balobanov et al. (2019). Moreover, the dynamic analysis of metal foam porous cylindrical microshells subjected to moving loads was presented by Mirjavadi et al. (2019) by following the SGT. One direction of interesting studies in the realm of higher-order continuum theories comes from the continualization of certain classes of mechanical metamaterials: structures formed by either various types of lattices or different fiber arrangements, for instance, can be seen as microarchitural solids having such effective properties that cannot be embedded by classical homogenization into the classical continuum descriptions. Instead, either higher-order derivatives of displacements or independent variables such as rotations must be involved in energy functionals. For this direction, we refer to some recent studies on lattice and cellular structures (Khakalo et al., 2018; Khakalo and Niiranen, 2018, 2019, 2020bib_Khakalo_and_Niiranen_2020bib_Khakalo_and_Niiranen_2019bib_Khakalo_and_Niiranen_2018) and pantographic structures (Dell'Isola et al., 2019b; Dell'Isola et al., 2019c). Finally, we note about an interesting but somewhat confusing issue: the standard beam, plate and shell models of the classical continuum mechanics can be considered as one kind of generalized continuum models as such. Namely, the well-known kinematical dimension reduction assumption for the axial displacement of Timoshenko beams, for instance, already introduces rotation as an independent variable aside deflection. In Euler–Bernoulli beams, in turn, rotation is constrained to be equal to the derivative of deflection. This naturally results in a second order derivative in the corresponding strain energy. As an example, we point out a study by Schulte et al. (2020) analyzing fiber-reinforced composite structures as Kirchoff–Love shells, as a theoretically solid continualization approach has shown that such a second gradient continuum framework (although being simply a classical shell model within the classical continuum mechanics) with a proper idenfication for the effective material parameters properly describes the mechanics of the fiber arrangement.

Despite the emphasis on analytical solutions in the early works, a diverse range of numerical studies based on different methods, such as the generalized differential quadrature (DQ) method (Ke et al., 2012; Ke and Wang, 2011; Ansari et al., 2016a; Hosseini et al., 2019), isogeometric analysis (IGA) (Fischer et al., 2011; Niiranen et al., 2016, 2017, 2019bib_Niiranen_et_al_2016bib_Niiranen_et_al_2019; Yaghoubi et al., 2018; Balobanov and Niiranen, 2018bib_Niiranen_et_al_2017; Thai et al., 2017) and the finite element (FE) method (Engel et al., 2002; Zervos et al., 2009; Zervos, 2008; Kwon and Lee, 2017; Dadgar-Rad, 2017; Ansari et al., 2015b, 2016bbib_Ansari_et_al_2015bbib_Ansari_et_al_2016b; Papanicolopulos et al., 2009; Farahmand et al., 2011; Torabi et al., 2018, 2019bib_Torabi_et_al_2019bib_Torabi_et_al_2018), have been carried out on the size-dependent mechanics of microstructures or microarchitectural structures. For example, the generalized DQ technique was applied by Ke et al. (2012) to perform size-dependent static and dynamic analyses for FG annular plates following the modified couple stress theory (MCST). Ansari et al. (2016a) outlined nonlinear postbuckling and vibration of microbeams based on Mindlin's SGT and the Levinson-Brickford-Reddy beam model employing a variational DQ method. IGA for membrane (Niiranen et al., 2016), beam (Niiranen et al., 2019; Yaghoubi et al., 2018; Balobanov and Niiranen, 2018), plate (Niiranen et al., 2017) and shell (Balobanov et al., 2019) structures within the SGT were presented by Niiranen and his co-authors, whereas IGA for microplates under the MSGT was presented by Thai and his co-authors (Thai et al., 2017).

In comparison to many other numerical approaches, the FE method provides perhaps the most comprehensive and versatile computational infrastructure to conduct numerical simulations on different aspects of science and engineering. However, in the case of the SGT, the presence of higher-order derivatives of displacements in the expression of the strain and kinetic energy functionals require higher-order finite elements to ensure the continuity requirements for conformity. As already shown within the SGT in (Balobanov et al., 2019; Niiranen et al., 2016, 2017, 2019bib_Niiranen_et_al_2016bib_Niiranen_et_al_2019; Yaghoubi et al., 2018; Balobanov and Niiranen, 2018bib_Niiranen_et_al_2017; Thai et al., 2017), the standard IGA provides continuity in a very natural and versatile way but not for multi-patch domains. Accordingly, various investigations have been published to study the performance of the FE method within the SGT. Different triangular and quadrilateral higher-order elements were presented by Zervos et al. (2009) to model SGT boundary value problems. Kwon et al. (Kwon and Lee, 2017) presented a quadrilateral element employing the Lagrange multiplier technique through a mixed formulation to consider the size-effects in the MCST. In order to simulate the mechanics of microplates within the SGT, bib_Ansari_et_al_2015bAnsari et al., 2015b, 2016bbib_Ansari_et_al_2016b proposed C^1-continuous triangular and quadrilateral elements. Besides, Papanicolopulos et al. (2009) introduced higher-order hexahedral elements based on Hermite's approximation functions, to numerically model the structural problems of the SGT. Recently, bib_Torabi_et_al_2019Torabi et al., 2018, 2019bib_Torabi_et_al_2018 developed tetrahedral and hexahedral elements to study the vibration of 3D structures under the SGT. The elements were developed by using the displacement field and its higher-order derivatives as nodal values in order to respond to the continuity requirements.

As the literature review above implies, in comparison to the studies regarding beam, plate and shell theories, only a few FE analyses have been carried out for 3D models. Besides, although some theoretical studies can be found (Javili et al., 2013), the number of studies focusing on geometrically nonlinear structural analysis is much smaller than the number of studies performed within the linear SGT. Moreover, most of the nonlinear SGT analyses (for instance (Ghayesh et al., 2013; Kahrobaiyan et al., 2011; Ansari et al., 2016a; Ansari et al., 2016b)) were presented according to the von Kármán geometric nonlinearity. Hence, the main purpose of this research is to highlight the nonlinear bending analysis of strain gradient plates based on two different structural models: the FSDT and the 3D theory. The von Kármán nonlinear kinematic relations and the nonlinear Green–Lagrange strain relations are adopted for the FSDT and the 3D theory, respectively. To facilitate the computational implementation of the SGT after briefly recalling its theoretical foundation (Section 2), the matrix-vector versions of the energy functionals are presented (Sections 3 and 4). Then, by relying on the principle of virtual work (Section 5), the nonlinear FE formulations of the different models are provided based on higher-order triangular and tetrahedral elements, respectively (Section 6). Finally, the Newton-Raphson method is used to solve the resulting nonlinear algebraic systems for following the corresponding displacement-load curves (Section 7). To study the differences between the proposed models and to demonstrate the reliability and efficiency of the related FE methods, nonlinear static bending of two different types of plate structures is analyzed, including convergence studies: a rectangular plate with a circular hole and an elliptical plate.

2. Mindlin's strain gradient theory

The details of Mindlin's SGT can be found in different studies (Mindlin, 1964; Ramezani, 2012; Ansari et al., 2016b; Papanicolopulos et al., 2009). Therefore, the main fundamentals of this theory are briefly presented in this section and the detailed matrix-vector relations are provided in Section 3. By following the SGT, the functional of the strain energy density is defined as a combination of the components of the strain (ε_{ij}) and strain gradient (κ_{ijk}) tensors as (Mindlin, 1964)

$$\widetilde{\mathscr{F}}=\frac{1}{2}\lambda\varepsilon_{ii}\varepsilon_{jj}+\mu\varepsilon_{ij}\varepsilon_{ij}+a_1\kappa_{kii}\kappa_{jjk}+a_2\kappa_{jji}\kappa_{kki}+a_3\kappa_{kii}\kappa_{kjj}+a_4\kappa_{ijk}\kappa_{ijk}+a_5\kappa_{ijk}\kappa_{kji} \tag{1}$$

with the following relations for the strain and strain gradient tensors:

$$\widetilde{\boldsymbol{\varepsilon}}=\frac{1}{2}\left(\nabla\mathbf{d}+(\nabla\mathbf{d})^{\mathrm{T}}+(\nabla\mathbf{d})^{\mathrm{T}}(\nabla\mathbf{d})\right),\ \varepsilon_{ij}=\frac{1}{2}\left(d_{i,j}+d_{j,i}+d_{k,i}d_{k,j}\right)=\varepsilon_{ji} \tag{2}$$

$$\widetilde{\boldsymbol{\kappa}}=\nabla\widetilde{\boldsymbol{\varepsilon}},\ \kappa_{ijk}=\varepsilon_{ij,k}=\kappa_{jik}$$

where d_i represents the displacement component in the coordinate direction i, λ and μ denote Lame's constants and a_m $(m=1,2,3,4,5)$ stand for the material parameters of the strain gradient effects. For clarity, the upper tilde refers to the standard tensor notation, used here for introducing the general framework, whereas the same letters without tildes are reserved for the corresponding vector notation preferred below on the way to the corresponding finite element formulations. By following the strain energy Eq. (1) and considering δ_{ij} as the Kronecker delta, the stress and double stress read as (Mindlin, 1964)

$$S_{ij}=S_{ji}=\frac{1}{2}\left(\frac{\partial\widetilde{\mathscr{F}}}{\partial\varepsilon_{ij}}+\frac{\partial\widetilde{\mathscr{F}}}{\partial\varepsilon_{ji}}\right)=\lambda\varepsilon_{kk}\delta_{ij}+2\mu\varepsilon_{ij} \tag{3}$$

$$\tau_{ijk}=\tau_{jik}=\frac{1}{2}\left(\frac{\partial\widetilde{\mathscr{F}}}{\partial\kappa_{ijk}}+\frac{\partial\widetilde{\mathscr{F}}}{\partial\kappa_{jik}}\right)=\frac{1}{2}a_1\left(\kappa_{ppi}\delta_{jk}+2\kappa_{kpp}\delta_{ij}+\kappa_{ppj}\delta_{ik}\right)+2a_2\kappa_{ppk}\delta_{ij}$$
$$+a_3\left(\kappa_{ipp}\delta_{jk}+\kappa_{jpp}\delta_{ik}\right)\quad+2a_4\kappa_{ijk}+a_5\left(\kappa_{kji}+\kappa_{kij}\right)$$

By introducing $\widetilde{\mathcal{C}}$ as the classical fourth-order elasticity tensor and $\widetilde{\mathcal{A}}$ as the sixth-order strain gradient tensor, the stress and double stress tensors, respectively, can be rewritten as

$$\widetilde{\mathbf{S}}=\widetilde{\mathcal{C}}:\widetilde{\boldsymbol{\varepsilon}},\ \widetilde{\boldsymbol{\tau}}=\widetilde{\mathcal{A}}\vdots\widetilde{\boldsymbol{\kappa}} \tag{4}$$

where $:$ and $\vdots$ denote the double and triple contractions, respectively. Now, by using the given relations, the strain energy density can be represented as

$$\widetilde{\mathscr{F}}=\frac{1}{2}\left(\widetilde{\boldsymbol{\varepsilon}}:\widetilde{\mathbf{S}}+\widetilde{\boldsymbol{\kappa}}\vdots\widetilde{\boldsymbol{\tau}}\right)=\frac{1}{2}\left(\widetilde{\boldsymbol{\varepsilon}}:\widetilde{\mathcal{C}}:\widetilde{\boldsymbol{\varepsilon}}+\widetilde{\boldsymbol{\kappa}}\vdots\widetilde{\mathcal{A}}\vdots\widetilde{\boldsymbol{\kappa}}\right) \tag{5}$$

In what follows, the matrix-vector forms of governing equations are first defined based on 3D elasticity, then for the corresponding FSDT plate model, and finally the detailed FE formulations are presented for both cases before comparative studies.

3. Three-dimensional elasticity theory

The Cartesian coordinate system (x,y,z) is employed to define the governing equations based on 3D elasticity and the displacement field is introduced as

$$U=\begin{bmatrix}u_x(x,y,z)\\u_y(x,y,z)\\u_z(x,y,z)\end{bmatrix} \tag{6}$$

with u_x,u_y,u_z as the displacements along the x,y,z coordinates. Now, by following the definition of the 3D Green–Lagrange strain tensor in the first relation of Eq. (2), the strain vector is expressed as

$$\varepsilon=\begin{bmatrix}\varepsilon_{xx} & \varepsilon_{yy} & \varepsilon_{zz} & \gamma_{yz} & \gamma_{xz} & \gamma_{xy}\end{bmatrix}^{\mathrm{T}}=\left(\mathbf{E}_e+\frac{1}{2}\mathbf{E}_e^n\right)U \tag{7}$$

with $\mathbf{E}_e$ and $\mathbf{E}_e^n$ as the linear (without any superscript) and nonlinear (superscript n) operators for the classical elasticity (subscript e) defined as

$$\mathbf{E}_e=\begin{bmatrix}\partial_x & 0 & 0\\0 & \partial_y & 0\\0 & 0 & \partial_z\\0 & \partial_z & \partial_y\\\partial_z & 0 & \partial_x\\\partial_y & \partial_x & 0\end{bmatrix}, \tag{8}$$

$$\mathbf{E}_e^n=\sum_{m=1}^{3}\mathbf{G}_{2m-1}U\mathbf{G}_{2m}+\mathbf{G}_{2m}U\mathbf{G}_{2m-1} \tag{9}$$

with

$$\mathbf{G}_{2m-1}=\mathbf{e}_m\otimes\begin{bmatrix}\partial_x\\\partial_y\\\partial_z\\\partial_y\\\partial_x\\\partial_x\end{bmatrix},\ \mathbf{G}_{2m}=\mathbf{e}_m\otimes\frac{1}{2}\begin{bmatrix}\partial_x\\\partial_y\\\partial_z\\2\partial_z\\2\partial_z\\2\partial_y\end{bmatrix},\ \mathbf{e}_m=\begin{bmatrix}\delta_{m1} & \delta_{m2} & \delta_{m3}\end{bmatrix},\quad m=1,2,3 \tag{10}$$

where "$\otimes$" symbolizes the Kronecker product and ● indicates the *diag* function. Also.

δ_{mi} $(i=1,2,3)$ is the Kronecker delta where $\delta_{mi}=1$ when $m=i$ and $\delta_{mi}=0$ when $m\neq i$. As an example, it can be considered that in Eq. (9), $\mathbf{e}_2=\begin{bmatrix}\delta_{21} & \delta_{22} & \delta_{23}\end{bmatrix}=\begin{bmatrix}0 & 1 & 0\end{bmatrix}$. Accordingly, by calculating the gradients of the strain components according to the second relation of Eq. (2), the strain gradient vector is given as (Torabi et al., 2018)

$$\boldsymbol{\kappa}=\begin{bmatrix}\boldsymbol{\kappa}_1\\\boldsymbol{\kappa}_2\\\boldsymbol{\kappa}_3\\\boldsymbol{\kappa}_4\end{bmatrix}=\left(\mathbf{E}_s+\frac{1}{2}\mathbf{E}_s^n\right)U, \tag{11}$$

where $\boldsymbol{\kappa}_i$ $(i=1,2,3,4)$ introduce the strain gradient components as vectors

$$\boldsymbol{\kappa}_1=\begin{bmatrix}\varepsilon_{xx,x}\\\varepsilon_{yy,x}\\\gamma_{yx,y}\\\varepsilon_{zz,x}\\\gamma_{zx,z}\end{bmatrix},\ \boldsymbol{\kappa}_2=\begin{bmatrix}\varepsilon_{yy,y}\\\varepsilon_{xx,y}\\\gamma_{xy,x}\\\varepsilon_{zz,y}\\\gamma_{zy,z}\end{bmatrix},\ \boldsymbol{\kappa}_3=\begin{bmatrix}\varepsilon_{zz,z}\\\varepsilon_{xx,z}\\\gamma_{xz,x}\\\varepsilon_{yy,z}\\\gamma_{yz,y}\end{bmatrix},\ \boldsymbol{\kappa}_4=\begin{bmatrix}\gamma_{xy,z}\\\gamma_{xz,y}\\\gamma_{zy,x}\end{bmatrix} \tag{12}$$

and $\mathbf{E}_s$ and $\mathbf{E}_s^n$, respectively, are the linear (without any superscript) and nonlinear (superscript n) matrix operators for the SGT (subscript s) defined as

$$\mathbf{E}_s=\begin{bmatrix}\mathbf{E}_s^1\\\mathbf{E}_s^2\\\mathbf{E}_s^3\\\mathbf{E}_s^4\end{bmatrix},\ \mathbf{E}_s^n=\sum_{m=1}^{3}\mathbf{Q}_{2m-1}U\mathbf{Q}_{2m}+\mathbf{Q}_{2m}U\mathbf{Q}_{2m-1}+\widehat{\mathbf{Q}}_{2m-1}U\widehat{\mathbf{Q}}_{2m}+\widehat{\mathbf{Q}}_{2m}U\widehat{\mathbf{Q}}_{2m-1} \tag{13}$$

in which the following matrix differential operators

$$\mathbf{E}_s^1=\begin{bmatrix}\partial_{xx} & 0 & 0\\0 & \partial_{yx} & 0\\\partial_{yy} & \partial_{xy} & 0\\0 & 0 & \partial_{zx}\\\partial_{zz} & 0 & \partial_{zx}\end{bmatrix},\ \mathbf{E}_s^2=\begin{bmatrix}0 & \partial_{yy} & 0\\\partial_{xy} & 0 & 0\\\partial_{yx} & \partial_{xx} & 0\\0 & 0 & \partial_{zy}\\0 & \partial_{zz} & \partial_{zy}\end{bmatrix},\ \mathbf{E}_s^3=\begin{bmatrix}0 & 0 & \partial_{zz}\\\partial_{xz} & 0 & 0\\\partial_{zx} & 0 & \partial_{xx}\\0 & \partial_{yz} & 0\\0 & \partial_{zy} & \partial_{yy}\end{bmatrix},\ \mathbf{E}_s^4=\begin{bmatrix}\partial_{yz} & \partial_{zx} & 0\\\partial_{yz} & 0 & \partial_{yx}\\0 & \partial_{zx} & \partial_{yx}\end{bmatrix} \tag{14}$$

are for the linear part, whereas

$$\mathbf{Q}_{2m}=\begin{bmatrix}\mathbf{Q}_{2m}^{1}\\ \mathbf{Q}_{2m}^{2}\\ \mathbf{Q}_{2m}^{3}\\ \mathbf{Q}_{2m}^{4}\end{bmatrix},\ \mathbf{Q}_{2m-1}=\begin{bmatrix}\mathbf{Q}_{2m-1}^{1}\\ \mathbf{Q}_{2m-1}^{2}\\ \mathbf{Q}_{2m-1}^{3}\\ \mathbf{Q}_{2m-1}^{4}\end{bmatrix},\ \widehat{\mathbf{Q}}_{2m}=\begin{bmatrix}\widehat{\mathbf{Q}}_{2m}^{1}\widehat{\mathbf{Q}}_{2m}^{2}\widehat{\mathbf{Q}}_{2m}^{3}\widehat{\mathbf{Q}}_{2m}^{4}\end{bmatrix},\ \widehat{\mathbf{Q}}_{2m-1}=\begin{bmatrix}\widehat{\mathbf{Q}}_{2m-1}^{1}\widehat{\mathbf{Q}}_{2m-1}^{2}\widehat{\mathbf{Q}}_{2m-1}^{3}\widehat{\mathbf{Q}}_{2m-1}^{4}\end{bmatrix} \tag{15}$$

with

$$\begin{cases}\mathbf{Q}_{2m-1}^{i}=\mathbf{e}_m\otimes\mathbf{L}_1^{i},\ \mathbf{Q}_{2m}^{i}=\mathbf{e}_m\otimes\mathbf{L}_2^{i},\\ \widehat{\mathbf{Q}}_{2m-1}^{i}=\mathbf{e}_m\otimes\mathbf{L}_3^{i},\ \widehat{\mathbf{Q}}_{2m}^{i}=\mathbf{e}_m\otimes\mathbf{L}_4^{i},\quad m=1,2,3\quad\text{and}\quad i=1,2,3,4\end{cases} \tag{16}$$

are the matrices for the nonlinear part with the following differential operators

$$\mathbf{L}_1^1=\begin{bmatrix}\partial_{xx}\\ \partial_{yx}\\ \partial_{yx}\\ \partial_{zx}\\ \partial_{zx}\end{bmatrix},\ \mathbf{L}_2^1=\begin{bmatrix}\partial_{x}\\ \partial_{y}\\ \partial_{y}\\ \partial_{z}\\ \partial_{z}\end{bmatrix},\ \mathbf{L}_3^1=\begin{bmatrix}0\\ 0\\ \partial_{yy}\\ 0\\ \partial_{zz}\end{bmatrix},\ \mathbf{L}_4^1=\begin{bmatrix}0\\ 0\\ \partial_{x}\\ 0\\ \partial_{x}\end{bmatrix} \tag{17}$$

$$\mathbf{L}_1^2=\begin{bmatrix}\partial_{yy}\\ \partial_{yx}\\ \partial_{yx}\\ \partial_{zy}\\ \partial_{zy}\end{bmatrix},\ \mathbf{L}_2^2=\begin{bmatrix}\partial_{y}\\ \partial_{x}\\ \partial_{x}\\ \partial_{z}\\ \partial_{z}\end{bmatrix},\ \mathbf{L}_3^2=\begin{bmatrix}0\\ 0\\ \partial_{xx}\\ 0\\ \partial_{zz}\end{bmatrix},\ \mathbf{L}_4^2=\begin{bmatrix}0\\ 0\\ \partial_{y}\\ 0\\ \partial_{y}\end{bmatrix} \tag{18}$$

$$\mathbf{L}_1^3=\begin{bmatrix}\partial_{zz}\\ \partial_{zx}\\ \partial_{zx}\\ \partial_{zy}\\ \partial_{zy}\end{bmatrix},\ \mathbf{L}_2^3=\begin{bmatrix}\partial_{z}\\ \partial_{x}\\ \partial_{x}\\ \partial_{y}\\ \partial_{y}\end{bmatrix},\ \mathbf{L}_3^3=\begin{bmatrix}0\\ 0\\ \partial_{xx}\\ 0\\ \partial_{yy}\end{bmatrix},\ \mathbf{L}_4^3=\begin{bmatrix}0\\ 0\\ \partial_{z}\\ 0\\ \partial_{z}\end{bmatrix} \tag{19}$$

$$\mathbf{L}_1^4=\begin{bmatrix}\partial_{yz}\\ \partial_{zy}\\ \partial_{yx}\end{bmatrix},\ \mathbf{L}_2^4=\begin{bmatrix}\partial_{x}\\ \partial_{x}\\ \partial_{z}\end{bmatrix},\ \mathbf{L}_3^4=\begin{bmatrix}\partial_{xz}\\ \partial_{xy}\\ \partial_{zx}\end{bmatrix},\ \mathbf{L}_4^4=\begin{bmatrix}\partial_{y}\\ \partial_{z}\\ \partial_{y}\end{bmatrix} \tag{20}$$

In order to make these compact matrix formulations more explicit, the linear and nonlinear parts of vector $\boldsymbol{\kappa}_1$ are expanded with details as examples. Based on Eqs. (10) and (12), the linear part of $\boldsymbol{\kappa}_1$ is written as

$$\boldsymbol{\kappa}_1^{\text{Linear}}=\begin{bmatrix}\varepsilon_{xx,x}\\ \varepsilon_{yy,x}\\ \gamma_{yx,y}\\ \varepsilon_{zz,x}\\ \gamma_{zx,z}\end{bmatrix}^{\text{Linear}}=\mathbf{E}_s^1U=\begin{bmatrix}\partial_{xx}&0&0\\ 0&\partial_{yx}&0\\ \partial_{yy}&\partial_{xy}&0\\ 0&0&\partial_{zx}\\ \partial_{zz}&0&\partial_{zx}\end{bmatrix}\begin{bmatrix}u_x\\ u_y\\ u_z\end{bmatrix}=\begin{bmatrix}u_{x,xx}\\ u_{y,yx}\\ u_{x,yy}+u_{y,xy}\\ u_{z,zx}\\ u_{x,zz}+u_{z,zx}\end{bmatrix} \tag{21}$$

In the same manner, the nonlinear part can be written as

$$\boldsymbol{\kappa}_1^{\text{Nonlinear}}=\frac{1}{2}\left(\sum_{m=1}^{3}\mathbf{Q}_{2m-1}^{1}U\mathbf{Q}_{2m}^{1}+\mathbf{Q}_{2m}^{1}U\mathbf{Q}_{2m-1}^{1}+\widehat{\mathbf{Q}}_{2m-1}^{1}U\widehat{\mathbf{Q}}_{2m}^{1}+\widehat{\mathbf{Q}}_{2m}^{1}U\widehat{\mathbf{Q}}_{2m-1}^{1}\right)U \tag{22}$$

First, according to Eqs. (16) and (17), the first term of the series of Eq. (22) is presented for $m=1$ as follows:

$$\begin{aligned}\mathbf{Q}_{2m-1}^{1}\Big|_{m=1}&=\mathbf{Q}_1^1=\mathbf{e}_1\otimes\mathbf{L}_1^1=\begin{bmatrix}\partial_{xx}&0&0\\ \partial_{yx}&0&0\\ \partial_{yx}&0&0\\ \partial_{zx}&0&0\\ \partial_{zx}&0&0\end{bmatrix}\mathbf{Q}_1^1U\\ &=\begin{bmatrix}\partial_{xx}&0&0\\ \partial_{yx}&0&0\\ \partial_{yx}&0&0\\ \partial_{zx}&0&0\\ \partial_{zx}&0&0\end{bmatrix}\begin{bmatrix}u_x\\ u_y\\ u_z\end{bmatrix}=\begin{bmatrix}u_{x,xx}\\ u_{x,yx}\\ u_{x,yx}\\ u_{x,zx}\\ u_{x,zx}\end{bmatrix}\\ &=\begin{bmatrix}u_{x,xx}&0&0&0&0\\ 0&u_{x,yx}&0&0&0\\ 0&0&u_{x,yx}&0&0\\ 0&0&0&u_{x,zx}&0\\ 0&0&0&0&u_{x,zx}\end{bmatrix},\ \mathbf{Q}_{2m}^{1}\Big|_{m=1}=\mathbf{Q}_2^1\\ &=\mathbf{e}_1\otimes\mathbf{L}_2^1=\begin{bmatrix}\partial_{x}&0&0\\ \partial_{y}&0&0\\ \partial_{y}&0&0\\ \partial_{z}&0&0\\ \partial_{z}&0&0\end{bmatrix},\end{aligned} \tag{23}$$

$$\left(\mathbf{Q}_{2m-1}^{1}U\mathbf{Q}_{2m}^{1}\Big|_{m=1}\right)U=\mathbf{Q}_1^1U\mathbf{Q}_2^1U=\begin{bmatrix}u_{x,xx}&0&0&0&0\\ 0&u_{x,yx}&0&0&0\\ 0&0&u_{x,yx}&0&0\\ 0&0&0&u_{x,zx}&0\\ 0&0&0&0&u_{x,zx}\end{bmatrix}\begin{bmatrix}\partial_{x}&0&0\\ \partial_{y}&0&0\\ \partial_{y}&0&0\\ \partial_{z}&0&0\\ \partial_{z}&0&0\end{bmatrix}\begin{bmatrix}u_x\\ u_y\\ u_z\end{bmatrix}=\begin{bmatrix}u_{x,xx}u_{x,x}\\ u_{x,yx}u_{x,y}\\ u_{x,yx}u_{x,y}\\ u_{x,zx}u_{x,z}\\ u_{x,zx}u_{x,z}\end{bmatrix} \tag{24}$$

Analogously, the other three terms in the sum of Eq. (22) can be presented for $m=1$ as follows:

$$\left(\mathbf{Q}_{2m}^{1}U\mathbf{Q}_{2m-1}^{1}\Big|_{m=1}\right)U=\mathbf{Q}_2^1U\mathbf{Q}_1^1U=\begin{bmatrix}u_{x,xx}u_{x,x}\\ u_{x,yx}u_{x,y}\\ u_{x,yx}u_{x,y}\\ u_{x,zx}u_{x,z}\\ u_{x,zx}u_{x,z}\end{bmatrix} \tag{25}$$

$$\left(\widehat{\mathbf{Q}}_{2m-1}^{1}U\widehat{\mathbf{Q}}_{2m}^{1}\Big|_{m=1}\right)U=\widehat{\mathbf{Q}}\,{}_1^1U\widehat{\mathbf{Q}}_2^1U=\begin{bmatrix}0\\ 0\\ u_{x,yy}u_{x,x}\\ 0\\ u_{x,zz}u_{x,x}\end{bmatrix} \tag{26}$$

$$\left(\widehat{\mathbf{Q}}_{2m}^{1}U\widehat{\mathbf{Q}}_{2m-1}^{1}\Big|_{m=1}\right)U=\widehat{\mathbf{Q}}\widehat{\mathbf{Q}}_2^1U\widehat{\mathbf{Q}}\widehat{\mathbf{Q}}_1^1U=\begin{bmatrix}0\\ 0\\ u_{x,yy}u_{x,x}\\ 0\\ u_{x,zz}u_{x,x}\end{bmatrix} \tag{27}$$

By considering Eqs. (24)–(27), and by following the same procedure for $m=2,\ 3$, the total expression for the nonlinear part of $\boldsymbol{\kappa}_1$can be expressed as

$$\boldsymbol{\kappa}_1^{\text{Nonlinear}} = \begin{bmatrix} u_{x,xx}u_{x,x} \\ u_{x,yx}u_{x,y} \\ u_{x,yx}u_{x,y} + u_{x,yy}u_{x,x} \\ u_{x,zx}u_{x,z} \\ u_{x,zx}u_{x,z} + u_{x,zz}u_{x,x} \end{bmatrix} + \begin{bmatrix} u_{y,xx}u_{y,x} \\ u_{y,yx}u_{y,y} \\ u_{y,yx}u_{y,y} + u_{y,yy}u_{y,x} \\ u_{y,zx}u_{y,z} \\ u_{y,zx}u_{y,z} + u_{y,zz}u_{y,x} \end{bmatrix} + \begin{bmatrix} u_{z,xx}u_{z,x} \\ u_{z,yx}u_{z,y} \\ u_{z,yx}u_{z,y} + u_{z,yy}u_{z,x} \\ u_{z,zx}u_{z,z} \\ u_{z,zx}u_{z,z} + u_{z,zz}u_{z,x} \end{bmatrix} \tag{28}$$

More details can be found in (Papanicolopulos et al., 2009). According to the proposed kinematic relations and by the use of the Voigt notation for the classical and higher-order constitutive relations defined in Eq. (3), the corresponding stress ($\mathbf{S}$) and double stress vectors ($\boldsymbol{\tau}$) are given as (Torabi et al., 2018)

$$\mathbf{S} = \mathcal{C}\varepsilon \quad \boldsymbol{\tau} = \mathcal{A}\boldsymbol{\kappa} \tag{29}$$

where $\mathcal{C}$ denotes the classical constitutive matrix defined based on the classical fourth-order elasticity tensor ($\widetilde{\mathcal{C}}$) and $\mathcal{A}$ stands for the generalized constitutive matrix defined by using the sixth-order strain gradient tensor ($\widetilde{\mathcal{A}}$) with the following relations:

$$\mathcal{C} = \begin{bmatrix} \lambda+2\mu & \lambda & \lambda & 0 & 0 & 0 \\ & \lambda+2\mu & \lambda & 0 & 0 & 0 \\ & & \lambda+2\mu & 0 & 0 & 0 \\ & & & \mu & 0 & 0 \\ & & & & \mu & 0 \\ \text{sym.} & & & & & \mu \end{bmatrix}, \quad \mathcal{A} = \begin{bmatrix} \mathcal{A}_1 & 0 & 0 & 0 \\ 0 & \mathcal{A}_1 & 0 & 0 \\ 0 & 0 & \mathcal{A}_1 & 0 \\ 0 & 0 & 0 & \mathcal{A}_2 \end{bmatrix} \tag{30}$$

in which

$$\mathcal{A}_1 = \begin{bmatrix} c_1 & c_4 & c_5 & c_4 & c_5 \\ & c_2 & c_6 & 2a_2 & a_1/2 \\ & & c_3 & a_1/2 & a_3/2 \\ & & & c_2 & c_6 \\ \text{sym.} & & & & c_3 \end{bmatrix}, \quad \mathcal{A}_2 = \begin{bmatrix} a_4 & a_5/2 & a_5/2 \\ & a_4 & a_5/2 \\ \text{sym.} & & a_4 \end{bmatrix} \tag{31}$$

where c_i ($i = 1, 2, \ldots, 6$) can be expressed by using the strain gradient material parameters as

$$c_1 = 2\sum_{i=1}^{5} a_i\,,\ c_2 = 2a_2 + 2a_4,\ c_3 = \frac{1}{2}(a_3 + 2a_4 + a_5)\ c_4 = a_1 + 2a_2,\ c_5 = \frac{1}{2}(a_1 + 2a_3),\ c_6 = \frac{1}{2}(a_1 + 2a_5) \tag{32}$$

4. Plate model

The governing equations for the nonlinear strain gradient plate model are presented based on the FSDT by using a Cartesian coordinate system of (x,y,z). By introducing $u_x^0,\ u_y^0, u_z^0$ as the in-plane (subscripts x, y) and out-of-plane (subscript z) displacements of the mid-plane and ψ_x, ψ_y as the rotations, the displacement field is expressed as

$$U = \begin{bmatrix} u_x(x,y,z) \\ u_y(x,y,z) \\ u_z(x,y,z) \end{bmatrix} = \mathbf{P}_0 U_0, \quad \mathbf{P}_0 = \begin{bmatrix} 1 & 0 & 0 & z & 0 \\ 0 & 1 & 0 & 0 & z \\ 0 & 0 & 1 & 0 & 0 \end{bmatrix}, \quad U_0 = \begin{bmatrix} u_x^0(x,y) \\ u_y^0(x,y) \\ u_z^0(x,y) \\ \psi_x(x,y) \\ \psi_y(x,y) \end{bmatrix} \tag{33}$$

The strain vector $\varepsilon = \begin{bmatrix} \varepsilon_{xx} & \varepsilon_{yy} & \gamma_{xy} & \gamma_{xz} & \gamma_{yz} \end{bmatrix}^{\mathrm{T}}$ is defined under the von Kármán nonlinear kinematic relations as follows (with superscript n denoting the nonlinear part):

$$\varepsilon = \begin{bmatrix} \varepsilon_{xx} & \varepsilon_{yy} & \gamma_{xy} & \gamma_{xz} & \gamma_{yz} \end{bmatrix}^{\mathrm{T}} = \left(\mathbf{P}_1 \overline{\mathbf{E}}_e + \frac{1}{2}\mathbf{P}_2 \overline{\mathbf{E}}_e^n \right) U_0, \tag{34}$$

in which

$$\mathbf{P}_1 = \begin{bmatrix} \mathbf{I}_{3\times 3} & z\mathbf{I}_{3\times 3} & 0 \\ 0 & 0 & \mathbf{I}_{2\times 2} \end{bmatrix}, \ \mathbf{P}_2 = \begin{bmatrix} \mathbf{I}_{3\times 3} \\ 0_{2\times 3} \end{bmatrix} \overline{\mathbf{E}}_e^n = \overline{\mathbf{G}}_1 U_0 \overline{\mathbf{G}}_2 + \overline{\mathbf{G}}_2 U_0 \overline{\mathbf{G}}_1 \tag{35}$$

with the following matrix operators:

$$\overline{\mathbf{E}}_e = \begin{bmatrix} \partial_x & 0 & 0 & 0 & 0 \\ 0 & \partial_y & 0 & 0 & 0 \\ \partial_y & \partial_x & 0 & 0 & 0 \\ 0 & 0 & 0 & \partial_x & 0 \\ 0 & 0 & 0 & 0 & \partial_y \\ 0 & 0 & 0 & \partial_y & \partial_x \\ 0 & 0 & \partial_x & 1 & 0 \\ 0 & 0 & \partial_y & 0 & 1 \end{bmatrix} \overline{\mathbf{G}}_1 = \begin{bmatrix} 0 & 0 & \partial_x & 0 & 0 \\ 0 & 0 & \partial_y & 0 & 0 \\ 0 & 0 & \partial_x & 0 & 0 \end{bmatrix}, \ \overline{\mathbf{G}}_2 = \frac{1}{2}\begin{bmatrix} 0 & 0 & \partial_x & 0 & 0 \\ 0 & 0 & \partial_y & 0 & 0 \\ 0 & 0 & 2\partial_y & 0 & 0 \end{bmatrix} \tag{36}$$

In Eq. (35), $\mathbf{I}_{n\times n}$ is the n-by-n identity matrix.

Now, by considering the introduced strain vector for the plate theory and by calculating the gradients of the strain components according to Eq. (2), the strain gradient vector is presented as (Ansari et al., 2016b)

$$\boldsymbol{\kappa} = \begin{bmatrix} \overline{\boldsymbol{\kappa}}_1 \\ \overline{\boldsymbol{\kappa}}_2 \\ \overline{\boldsymbol{\kappa}}_3 \\ \overline{\boldsymbol{\kappa}}_4 \end{bmatrix} = \left(\mathbf{P}_3 \overline{\mathbf{E}}_s + \frac{1}{2}\mathbf{P}_4 \overline{\mathbf{E}}_s^n \right) U_0, \tag{37}$$

with

$$\overline{\boldsymbol{\kappa}}_1 = \begin{bmatrix} \varepsilon_{xx,x} \\ \varepsilon_{yy,x} \\ \gamma_{yx,y} \end{bmatrix}, \ \overline{\boldsymbol{\kappa}}_2 = \begin{bmatrix} \varepsilon_{yy,y} \\ \varepsilon_{xx,y} \\ \gamma_{xy,x} \end{bmatrix}, \ \overline{\boldsymbol{\kappa}}_3 = \begin{bmatrix} \varepsilon_{xx,z} \\ \gamma_{xz,x} \\ \varepsilon_{yy,z} \\ \gamma_{yz,y} \end{bmatrix}, \ \overline{\boldsymbol{\kappa}}_4 = \begin{bmatrix} \gamma_{xy,z} \\ \gamma_{yz,x} \\ \gamma_{zx,y} \end{bmatrix} \tag{38}$$

and

$$\overline{\mathbf{E}}_s = \begin{bmatrix} \overline{\mathbf{E}}_s^1 \\ \overline{\mathbf{E}}_s^2 \\ \overline{\mathbf{E}}_s^3 \\ \overline{\mathbf{E}}_s^4 \\ \overline{\mathbf{E}}_s^5 \\ \overline{\mathbf{E}}_s^6 \end{bmatrix}, \ \overline{\mathbf{E}}_s^n = \overline{\mathbf{Q}}_1 U_0 \overline{\mathbf{Q}}_2 + \overline{\mathbf{Q}}_2 U_0 \overline{\mathbf{Q}}_1 \mathbf{P}_3$$

$$= \begin{bmatrix} \mathbf{I}_{3\times 3} & z\mathbf{I}_{3\times 3} & 0 & 0 & 0 & 0 \\ 0 & 0 & \mathbf{I}_{3\times 3} & z\mathbf{I}_{3\times 3} & 0 & 0 \\ 0 & 0 & 0 & 0 & \mathbf{I}_{4\times 4} & 0 \\ 0 & 0 & 0 & 0 & 0 & \mathbf{I}_{3\times 3} \end{bmatrix}, \mathbf{P}_4 = \begin{bmatrix} \mathbf{p}^* & 0 \\ 0 & \mathbf{p}^* \\ 0_{7\times 4} & 0_{7\times 4} \end{bmatrix}, \ \mathbf{p}^* = \begin{bmatrix} 1 & 0 & 0 & 0 \\ 0 & 1 & 0 & 0 \\ 0 & 0 & 1 & 1 \end{bmatrix} \tag{39}$$

in which the following differential operators are employed:

$$\overline{\mathbf{E}}_s^1=\begin{bmatrix}\partial_{xx}&0&0&0&0\\0&\partial_{xy}&0&0&0\\\partial_{yy}&\partial_{xy}&0&0&0\end{bmatrix},\ \overline{\mathbf{E}}_s^2=\begin{bmatrix}0&0&0&\partial_{xx}&0\\0&0&0&0&\partial_{xy}\\0&0&0&\partial_{yy}&\partial_{xy}\end{bmatrix}\overline{\mathbf{E}}_s^3=\begin{bmatrix}0&\partial_{yy}&0&0&0\\\partial_{xy}&0&0&0&0\\\partial_{xy}&\partial_{xx}&0&0&0\end{bmatrix},\ \overline{\mathbf{E}}_s^4=\begin{bmatrix}0&0&0&0&\partial_{yy}\\0&0&0&\partial_{xy}&0\\0&0&0&\partial_{xy}&\partial_{xx}\end{bmatrix}\overline{\mathbf{E}}_s^5=\begin{bmatrix}0&0&0&\partial_{x}&0\\0&0&\partial_{xx}&\partial_{x}&0\\0&0&0&0&\partial_{y}\\0&0&\partial_{yy}&0&\partial_{y}\end{bmatrix},\quad \overline{\mathbf{E}}_s^6=\begin{bmatrix}0&0&0&\partial_{y}&\partial_{x}\\0&0&\partial_{xy}&0&\partial_{x}\\0&0&\partial_{xy}&\partial_{y}&0\end{bmatrix} \tag{40}$$

$$\overline{\mathbf{Q}}_i=\begin{bmatrix}0&0&\overline{\mathbf{L}}_i&0&0\end{bmatrix},\quad i=1,2\overline{\mathbf{L}}_1=\begin{bmatrix}\partial_x\\\partial_y\\\partial_x\\\partial_y\\\partial_y\\\partial_x\\\partial_y\\\partial_x\end{bmatrix},\ \overline{\mathbf{L}}_2=\begin{bmatrix}\partial_{xx}\\\partial_{xy}\\\partial_{yy}\\\partial_{xy}\\\partial_{yy}\\\partial_{xy}\\\partial_{xx}\\\partial_{xy}\end{bmatrix}, \tag{41}$$

In order to give some more details on the presented matrix formulations, an expanded form of the linear and nonlinear parts of vector $\overline{\boldsymbol{\kappa}}_1$ are represented as examples. Based on Eqs. (37)–(39) and by considering the linear matrix form differential operators from Eq. (40), the linear part of $\overline{\boldsymbol{\kappa}}_1$ can be presented as

$$\overline{\boldsymbol{\kappa}}_1^{\text{Linear}}=\begin{bmatrix}\varepsilon_{xx,x}\\\varepsilon_{yy,x}\\\gamma_{yx,y}\end{bmatrix}^{\text{Linear}}=\left(\mathbf{I}_{3\times3}\overline{\mathbf{E}}_s^1+z\mathbf{I}_{3\times3}\overline{\mathbf{E}}_s^2\right)U_0=\left(\begin{bmatrix}\partial_{xx}&0&0&0&0\\0&\partial_{xy}&0&0&0\\\partial_{yy}&\partial_{xy}&0&0&0\end{bmatrix}+z\begin{bmatrix}0&0&0&\partial_{xx}&0\\0&0&0&0&\partial_{xy}\\0&0&0&\partial_{yy}&\partial_{xy}\end{bmatrix}\right)\begin{bmatrix}u_x^0\\u_y^0\\u_z^0\\\psi_x\\\psi_y\end{bmatrix}=\begin{bmatrix}u_{x,xx}^0+z\psi_{x,xx}\\u_{y,xy}^0+z\psi_{y,xy}^0\\u_{x,yy}^0+u_{y,xy}^0+z\left(\psi_{x,yy}+\psi_{y,xy}^0\right)\end{bmatrix} \tag{42}$$

By following a similar procedure for the nonlinear part according to Eqs. (37) and (39), the nonlinear part can be written as

$$\overline{\boldsymbol{\kappa}}_1^{\text{Nonlinear}}=\frac{1}{2}[\mathbf{p}^*\ \ 0_{3\times4}]\left(\overline{\mathbf{Q}}_1U_0\overline{\mathbf{Q}}_2+\overline{\mathbf{Q}}_2U_0\overline{\mathbf{Q}}_1\right)U_0 \tag{43}$$

By taking the first relation of Eq. (41) into account, one can write

$$\overline{\mathbf{Q}}_1=\begin{bmatrix}0&0&\partial_x&0&0\\0&0&\partial_y&0&0\\0&0&\partial_x&0&0\\0&0&\partial_y&0&0\\0&0&\partial_y&0&0\\0&0&\partial_x&0&0\\0&0&\partial_y&0&0\\0&0&\partial_x&0&0\end{bmatrix},\ \overline{\mathbf{Q}}_2=\begin{bmatrix}0&0&\partial_{xx}&0&0\\0&0&\partial_{xy}&0&0\\0&0&\partial_{yy}&0&0\\0&0&\partial_{xy}&0&0\\0&0&\partial_{yy}&0&0\\0&0&\partial_{xy}&0&0\\0&0&\partial_{xx}&0&0\\0&0&\partial_{xy}&0&0\end{bmatrix} \tag{44}$$

$$\overline{\mathbf{Q}}_1U_0=\begin{bmatrix}0&0&\partial_x&0&0\\0&0&\partial_y&0&0\\0&0&\partial_x&0&0\\0&0&\partial_y&0&0\\0&0&\partial_y&0&0\\0&0&\partial_x&0&0\\0&0&\partial_y&0&0\\0&0&\partial_x&0&0\end{bmatrix}\begin{bmatrix}u_x^0\\u_y^0\\u_z^0\\\psi_x\\\psi_y\end{bmatrix}=\begin{bmatrix}u_{z,x}^0\\u_{z,y}^0\\u_{z,x}^0\\u_{z,y}^0\\u_{z,y}^0\\u_{z,x}^0\\u_{z,y}^0\\u_{z,x}^0\end{bmatrix}=\begin{bmatrix}u_{z,x}^0&0&0&0&0&0&0&0\\0&u_{z,y}^0&0&0&0&0&0&0\\0&0&u_{z,x}^0&0&0&0&0&0\\0&0&0&u_{z,y}^0&0&0&0&0\\0&0&0&0&u_{z,y}^0&0&0&0\\0&0&0&0&0&u_{z,x}^0&0&0\\0&0&0&0&0&0&u_{z,y}^0&0\\0&0&0&0&0&0&0&u_{z,x}^0\end{bmatrix} \tag{45}$$

$$\overline{\mathbf{Q}}_2U_0=\begin{bmatrix}0&0&\partial_{xx}&0&0\\0&0&\partial_{xy}&0&0\\0&0&\partial_{yy}&0&0\\0&0&\partial_{xy}&0&0\\0&0&\partial_{yy}&0&0\\0&0&\partial_{xy}&0&0\\0&0&\partial_{xx}&0&0\\0&0&\partial_{xy}&0&0\end{bmatrix}\begin{bmatrix}u_x^0\\u_y^0\\u_z^0\\\psi_x\\\psi_y\end{bmatrix}=\begin{bmatrix}u_{z,xx}^0\\u_{z,xy}^0\\u_{z,yy}^0\\u_{z,xy}^0\\u_{z,yy}^0\\u_{z,xy}^0\\u_{z,xx}^0\\u_{z,xy}^0\end{bmatrix}=\begin{bmatrix}u_{z,xx}^0&0&0&0&0&0&0&0\\0&u_{z,xy}^0&0&0&0&0&0&0\\0&0&u_{z,yy}^0&0&0&0&0&0\\0&0&0&u_{z,xy}^0&0&0&0&0\\0&0&0&0&u_{z,yy}^0&0&0&0\\0&0&0&0&0&u_{z,xy}^0&0&0\\0&0&0&0&0&0&u_{z,xx}^0&0\\0&0&0&0&0&0&0&u_{z,xy}^0\end{bmatrix}, \tag{46}$$

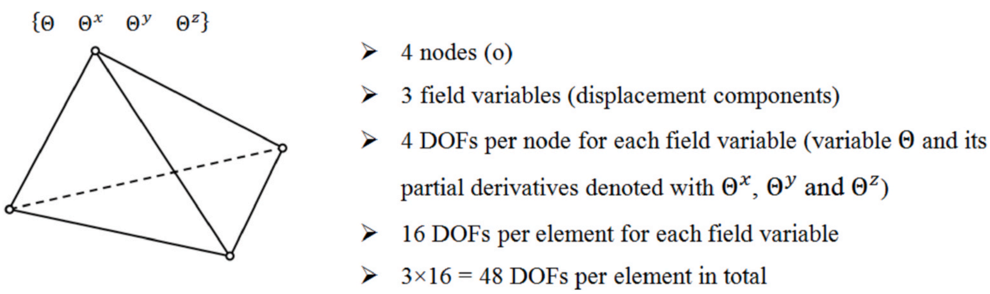

Fig. 1. Details of the quasi-C^1-continuous 4-node tetrahedral element.

By substituting Eqs. (44)–(46) into (43) and by considering matrix $\mathbf{p}^*$ from Eq. (39), the nonlinear part of $\overline{\boldsymbol{\kappa}}_1$ takes the form

$$\overline{\boldsymbol{\kappa}}_1^{\text{Nonlinear}} = \begin{bmatrix} u^0_{z,x}u^0_{z,xx} \\ u^0_{z,y}u^0_{z,xy} \\ u^0_{z,x}u^0_{z,yy} + u^0_{z,y}u^0_{z,xy} \end{bmatrix} \tag{47}$$

More details can be found in (Ansari et al., 2016b). Next, by using the Voigt notation for the classical and higher-order constitutive relations defined in Eq. (3), the stress and double stress vectors can be written as follows (Ansari et al., 2016b):

$$\mathbf{S} = \mathcal{C}\varepsilon \;\; \boldsymbol{\tau} = \mathcal{A}\boldsymbol{\kappa} \tag{48}$$

with

$$\mathcal{C} = \begin{bmatrix} \lambda+2\mu & \lambda & 0 & 0 & 0 \\ \lambda & \lambda+2\mu & 0 & 0 & 0 \\ 0 & 0 & \mu & 0 & 0 \\ 0 & 0 & 0 & \mu & 0 \\ 0 & 0 & 0 & 0 & \mu \end{bmatrix}, \tag{49}$$

$$\mathcal{A} = \begin{bmatrix} \overline{\mathcal{A}}_1 & 0 & 0 & 0 \\ 0 & \overline{\mathcal{A}}_1 & 0 & 0 \\ 0 & 0 & \overline{\mathcal{A}}_2 & 0 \\ 0 & 0 & 0 & \overline{\mathcal{A}}_3 \end{bmatrix} \tag{50}$$

where

$$\overline{\mathcal{A}}_1 = \begin{bmatrix} c_1 & c_4 & c_5 \\ c_4 & c_2 & c_6 \\ c_5 & c_6 & c_3 \end{bmatrix}, \overline{\mathcal{A}}_3 = \begin{bmatrix} c_2 & c_6 & 2a_2 & a_1/2 \\ c_6 & c_3 & a_1/2 & a_3/2 \\ 2a_2 & a_1/2 & c_2 & c_6 \\ a_1/2 & a_3/2 & c_6 & c_3 \end{bmatrix}, \overline{\mathcal{A}}_3 = \begin{bmatrix} a_4 & a_5/2 & a_5/2 \\ a_5/2 & a_4 & a_5/2 \\ a_5/2 & a_5/2 & a_4 \end{bmatrix}, \tag{51}$$

Note that coefficients c_i ($i = 1, 2, \ldots, 6$) have been defined in Eq. (32).

5. Principle of virtual work

Introducing $\mathscr{T}$ and V, respectively, as the strain energy and the potential energy of external forces, the minimum of the total potential energy principle gives the standard identity $\delta\mathscr{T} - \delta V = 0$ with δ symbolizing the first variation. By considering W as the work done by the external forces, one can write $\delta V = -\delta W$ for conservative forces giving

$$\delta\mathscr{T} + \delta W = 0 \tag{52}$$

On the basis of the strain energy density of Eq. (1) and the vectors of strain, stress, strain gradient and double stress, the first variation of the total strain energy is represented as

$$\delta\mathscr{T} = \delta\int_V \widetilde{\mathscr{T}} dV = \int_V \left(\delta\varepsilon^{\mathrm{T}}\mathbf{S} + \delta\boldsymbol{\kappa}^{\mathrm{T}}\boldsymbol{\tau}\right) dV = \int_V \left(\delta\varepsilon^{\mathrm{T}}\mathcal{C}\varepsilon + \delta\boldsymbol{\kappa}^{\mathrm{T}}\mathcal{A}\boldsymbol{\kappa}\right) dV \tag{53}$$

The first variations of the strain and strain gradient vectors of the 3D model and the plate model are, respectively,

$$\delta\varepsilon = \left(\mathbf{E}_e + \mathbf{E}_e^n\right)\delta U, \;\; \delta\boldsymbol{\kappa} = \left(\mathbf{E}_s + \mathbf{E}_s^n\right)\delta U \tag{54}$$

$$\delta\varepsilon = \left(\mathbf{P}_1\overline{\mathbf{E}}_e + \mathbf{P}_2\overline{\mathbf{E}}_e^n\right)U_0, \;\; \delta\boldsymbol{\kappa} = \left(\mathbf{P}_3\overline{\mathbf{E}}_s + \mathbf{P}_4\overline{\mathbf{E}}_s^n\right)U_0 \tag{55}$$

Regarding the plate formulation, it is worth noting that – similarly to the linear part of the standard strain vector – the strain gradient vector preserves the in-plane (stretching) components of the displacements field decoupled from the out-of-plane displacement and rotation (bending) components (cf. Eq. (42)). Instead, as the nonlinear part of the standard strain couples some of the stretching and bending components – implying the requirement of a complete FSDT plate model of five field variables – the nonlinear part of the strain gradient further complicates this coupling between the stretching and bending components through the higher-order derivatives of these components.

Besides the strain energy, by considering $\mathbf{f}$ and $\mathbf{p}$ as the vectors of the given body and surface forces, one can write the work done by the external forces for the 3D model as

$$\delta W = \int_V \delta U^{\mathrm{T}}\mathbf{f}\, dV + \int_A \delta U^{\mathrm{T}}\mathbf{p}\, dA \tag{56}$$

The corresponding relation for the plate model can be written accordingly.

6. Finite element formulations

The finite element discretization procedure is formulated in this section for large-amplitude strain gradient bending analysis based on both the 3D and the plate model. By following the fundamentals of the FE method, the structure is discretized into elements. If W_e and $\mathscr{T}_e$ stand for the work of external forces and strain energy of the element, respectively, the total counterparts are

$$W = \sum_{e=1}^{n} W_e, \;\; \mathscr{T} = \sum_{e=1}^{n} \mathscr{T}_e \tag{57}$$

where n presents the number of elements. In what follows, the detailed FE formulations for the 3D and plate models are provided.

6.1. FE formulation for 3D model

To numerically model the 3D problem via the FE method, the quasi C^1-continuous 4-node tetrahedral element introduced in (Torabi et al., 2019) was employed. The local volume coordinate (LVC) system (L_1, L_2, L_3, L_4) and a sample scalar field (θ) are used to present the governing equations of the element. As demonstrated in Fig. 1 and to respond to the continuity requirement, the values of the field (Θ_i) and the first-order

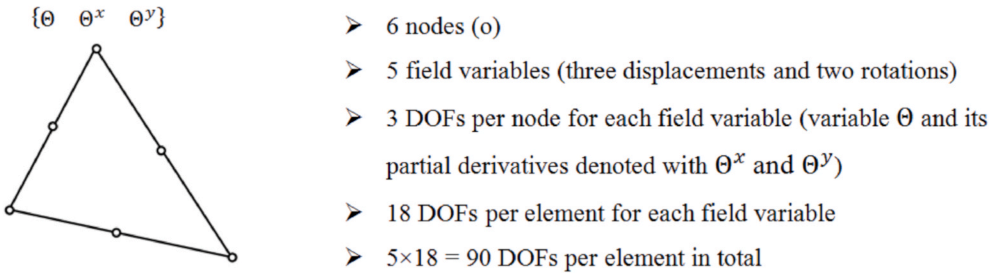

Fig. 2. Details of the quasi-C^1-continuous 6-node triangular element.

derivatives (Θ_i^x, Θ_i^y, Θ_i^z) are regarded as the nodal values:

$$\theta(\mathbf{L}_i)=\Theta_i,\ \frac{\partial\theta}{\partial x}\Big|_{\mathbf{L}=\mathbf{L}_i}=\Theta_i^x,\ \frac{\partial\theta}{\partial y}\Big|_{\mathbf{L}=\mathbf{L}_i}=\Theta_i^y,\quad \frac{\partial\theta}{\partial z}\Big|_{\mathbf{L}=\mathbf{L}_i}=\Theta_i^z\quad (i=1,2,3,4) \tag{58}$$

where $\mathbf{L}_i=[L_1^i\ L_2^i\ L_3^i\ L_4^i]^{\mathrm{T}}$ stands for the vector of the LVCs at node i. Based on the proposed element, the scalar field can be approximated within each element in terms of the LVCs as

$$\theta(\mathbf{L})=\ \mathbf{R}(\mathbf{L})q \tag{59}$$

where $\mathbf{R}(\mathbf{L})$ is the corresponding 1×16 vector of base functions and q is the 16×1 vector of unknowns presented as

$$\mathbf{R}(\mathbf{L})=\left[\mathbf{R}^0\ \ \mathbf{R}^1\ \ \mathbf{R}^2\ \ \mathbf{R}^3\ \ \mathbf{R}^4\right]q=[q_1\ q_2\ q_3\ \dots\ q_{16}]^{\mathrm{T}} \tag{60}$$

with

$$\mathbf{R}^0=\left[R_1^0\ \ R_2^0\ \ R_3^0\ \ R_4^0\right], \tag{61}$$

$$R_p^0=3L_p^2-2L_p^3+\sum_{\substack{1\le q\le4\\ q\ne p}}\frac{4D_pD_q^{\mathrm{T}}}{3|D_q|}t_q,\ (p=1,2,3,4)$$

and

$$\mathbf{R}^p=[R_1^p\ \ R_2^p\ \ R_3^p]=\sum_{1\le r\ne p\le4}\left\{L_p^2L_r+\frac{|D_r|}{9}t_r+\sum_{\substack{1\le q\le4\\ q\ne p}}\frac{(2D_p+D_r)D_q^T}{9|D_q|}t_q\right\}(b_r-b_p),\quad (p=1,2,3,4) \tag{62}$$

where

$$t_p=\frac{9}{4|D_p|}\left(\sum_{\substack{1\le r<q<s\le4\\ r\ne p,\ q\ne p,\ s\ne p}}L_rL_qL_s-L_p\sum_{\substack{1\le r<q\le4\\ r\ne p,\ q\ne p}}L_rL_q\right),\ (p=1,2,3,4)b_1=[0\ 0\ 0],\ b_2=[1\ 0\ 0],\ b_3=[0\ 1\ 0],\ b_4=[0\ 0\ 1]D_1=\ -[1\ 1\ 1],\ D_2=[1\ 0\ 0],\ D_3=[0\ 1\ 0],\ D_4=[0\ 0\ 1], \tag{63}$$

Since the 4-node tetrahedral element has been considered and each node has four nodal values (for each variable) including the field variable (Θ_i) and its first-order derivatives (Θ_i^x, Θ_i^y, Θ_i^z), $\mathbf{R}(\mathbf{L})$ and q in Eq. (60) contain 16 terms. It means that the number of degrees of freedom (DOF) for each field variable within the element is 16. By substituting Eq. (59) into (58) and solving the resultants for the unknown vector q, one can find the vector of shape functions for the quasi-C^1-continuous 4-node tetrahedral element ($\mathbf{N}_e=[\mathcal{N}_1\ \ \mathcal{N}_2\ \ \cdots\ \ \mathcal{N}_{16}]$). It should be pointed out that in the case of the 3D elasticity theory, there are three field variables (u_xu_y, u_z) and, consequently, there will be a total of $3\times16=48$ DOFs per element (please see Fig. 1). More details can be found in (Torabi et al., 2019).

Now, the approximation of the vector of the displacement field is given as

$$U=\mathcal{N}\mathbf{q} \tag{64}$$

$$\mathcal{N}=\begin{bmatrix}\mathcal{N}_1 & 0 & 0 & & \mathcal{N}_{16} & 0 & 0\\ 0 & \mathcal{N}_1 & 0 & \dots & 0 & \mathcal{N}_{16} & 0\\ 0 & 0 & \mathcal{N}_1 & & 0 & 0 & \mathcal{N}_{16}\end{bmatrix}=\begin{bmatrix}\mathbf{N}_e\otimes\mathbf{e}_1\\ \mathbf{N}_e\otimes\mathbf{e}_2\\ \mathbf{N}_e\otimes\mathbf{e}_3\end{bmatrix} \tag{65}$$

where $\mathbf{q}$ denotes the vector of nodal values. Substituting Eq. (64) into (7), (11) and (54) gives the approximation of the strain vector, strain gradient vector and their first variations as follows:

$$\varepsilon=\left(\mathbf{B}_e+\frac{1}{2}\mathbf{B}_e^n\right)\mathbf{q},\ \boldsymbol{\kappa}=\left(\mathbf{B}_s+\frac{1}{2}\mathbf{B}_s^n\right)\mathbf{q}\ \delta\varepsilon=\left(\mathbf{B}_e+\mathbf{B}_e^n\right)\delta\mathbf{q},\ \delta\boldsymbol{\kappa}=\left(\mathbf{B}_s+\mathbf{B}_s^n\right)\delta\mathbf{q} \tag{66}$$

in which the linear and nonlinear (superscript n) strain and strain gradient matrices are represented as

$$\mathbf{B}_e = \mathbf{E}_e\mathcal{N},\ \mathbf{B}_s = \mathbf{E}_s\mathcal{N},\ \mathbf{B}_e^n = \sum_{m=1}^{3}\mathbf{D}_{2m-1}\mathbf{q}\mathbf{D}_{2m} + \mathbf{D}_{2m}\mathbf{q}\mathbf{D}_{2m-1},\ \mathbf{B}_s^n = \sum_{m=1}^{3}\mathbf{M}_{2m-1}\mathbf{q}\mathbf{M}_{2m} + \mathbf{M}_{2m}\mathbf{q}\mathbf{M}_{2m-1} + \widehat{\mathbf{M}}_{2m-1}\mathbf{q}\widehat{\mathbf{M}}_{2m} + \widehat{\mathbf{M}}_{2m}\mathbf{q}\widehat{\mathbf{M}}_{2m-1} \tag{67}$$

with

$$\mathbf{D}_i = \mathbf{G}_i\mathcal{N},\ \mathbf{M}_i = \mathbf{Q}_i\mathcal{N},\ \widehat{\mathbf{M}}_i = \widehat{\mathbf{Q}}_i\mathcal{N},\ (i=1,2,\ldots,6) \tag{68}$$

Now, the strain energy is simplified by using Eqs. (53) and (66) as follows:

$$\delta\mathcal{T}_e = \delta\mathbf{q}^{\mathrm{T}}\mathbf{K}\mathbf{q} \tag{69}$$

continuity requirement between the elements:

$$\theta(\mathbf{L}_i) = \Theta_i,\ \frac{\partial\theta}{\partial x}\Big|_{\mathbf{L}=\mathbf{L}_i} = \Theta_i^x,\ \frac{\partial\theta}{\partial y}\Big|_{\mathbf{L}=\mathbf{L}_i} = \Theta_i^y,\ \left(i=1,2,\ldots,6\right) \tag{76}$$

in which $\mathbf{L}_i = [L_1^i\ L_2^i\ L_3^i]^{\mathrm{T}}$ gives the vector of the LACs at node i.

Based on the proposed element, the scalar field can be approximated within each element in terms of the LACs as

$$\theta(\mathbf{L}) = \overline{\mathbf{R}}(\mathbf{L})\overline{q} \tag{77}$$

where $\overline{\mathbf{R}}(\mathbf{L})$ denoting the corresponding 1×18 vector of the basis functions and $\overline{q}$ standing for the 18×1 vector of unknowns are presented as

$$\overline{\mathbf{R}}(\mathbf{L}) = \left[L_1\ L_2\ L_3\ L_1L_2\ L_2L_3\ L_1L_3\ L_1^2L_2\ L_2^2L_3\ L_3^2L_1\ L_1^2L_2^2\ L_2^2L_3^2\ L_3^2L_1^2\ L_1^3L_2\ L_2^3L_3\ L_3^3L_1\ L_1^4L_2\ L_2^4L_3\ L_3^4L_1\right],\ \overline{q} = \left[\overline{q}_1\ \overline{q}_2\ \overline{q}_3\ \ldots\ \overline{q}_{18}\right]^{\mathrm{T}} \tag{78}$$

in which

$$\mathbf{K} = \mathbf{K}_l + \frac{1}{2}\mathbf{K}_{nl} + \frac{1}{3}\mathbf{K}_{nl}^* \tag{70}$$

with

$$\mathbf{K}_l = \int_V (\mathbf{B}_e^{\mathrm{T}}\mathcal{C}\mathbf{B}_e + \mathbf{B}_s^{\mathrm{T}}\mathcal{A}\mathbf{B}_s)dV,\ \mathbf{K}_{nl} = \int_V (\mathbf{B}_e^{\mathrm{T}}\mathcal{C}\mathbf{B}_e^n + 2\mathbf{B}_e^{n\mathrm{T}}\mathcal{C}\mathbf{B}_e + \mathbf{B}_s^{\mathrm{T}}\mathcal{A}\mathbf{B}_s^n + 2\mathbf{B}_s^{n\mathrm{T}}\mathcal{A}\mathbf{B}_s)dV\mathbf{K}_{nl}^* = \frac{3}{2}\int_V (\mathbf{B}_e^{n\mathrm{T}}\mathcal{C}\mathbf{B}_e^n + \mathbf{B}_s^{n\mathrm{T}}\mathcal{A}\mathbf{B}_s^n)dV \tag{71}$$

in which subscript l refers to the purely linear part (including the classical and SGT terms) and subscript nl refers to the nonlinear parts, with an asterisk as a superscript referring to the purely nonlinear portion. Besides, the first variation of the work done by the external forces is presented by considering Eq. (64) into (56) as

$$\delta W_e = \delta\mathbf{q}^{\mathrm{T}}\int_V \mathcal{N}^{\mathrm{T}}\mathbf{f}\,dV + \delta\mathbf{q}^{\mathrm{T}}\int_A \mathcal{N}^{\mathrm{T}}\mathbf{p}\,dA \tag{72}$$

which can be simplified to

$$\delta W_e = \delta\mathbf{q}^{\mathrm{T}}\mathbf{F} \tag{73}$$

with

$$\mathbf{F} = \int_V \mathcal{N}^{\mathrm{T}}\mathbf{f}\,dV + \int_A \mathcal{N}^{\mathrm{T}}\mathbf{p}\,dA \tag{74}$$

Next, the variations of the strain energy and work of external forces are substituted from Eqs. (69) and (73) into Eq. (52) which gives the final FE equation system via an appropriate assembly procedure for the corresponding global stiffness matrix, displacement vector and force vector in the standard form (including the geometric nonlinearities according to Eqs. (70)–(71), i.e., the dependency of $\mathbb{K}$ on q)

$$\mathbb{K}q + \mathbb{F} = 0 \tag{75}$$

6.2. FE formulation for plate model

The FE formulation for the plate model is presented by using the higher-order 6-node triangular element. The description of the element is given in terms of the local area coordinate (LAC) system of (L_1, L_2, L_3) for a sample scalar field (θ) serving as an example variable (see Section 4). As can be seen in Fig. 2, the nodal values are the values of the field variable (Θ_i) and its first-order derivatives (Θ_i^x, Θ_i^y) to respond to the

Since the 6-node triangular element has been considered and each node has three nodal values (for each variable) including the field variable (Θ_i) and its first-order derivatives (Θ_i^x, Θ_i^y), $\overline{\mathbf{R}}(\mathbf{L})$ and $\overline{q}$ in Eq. (78) contain $6\times3=18$ terms. It means that the number of degrees of freedom (DOF) for each field variable within the element is 18. By substituting Eq. (77) into (76) and solving the resultants for the unknown vector $\overline{q}$, the vector of shape functions ($\overline{\mathbf{N}}_e = \left[\mathcal{N}_1\ \ \mathcal{N}_2\ \ \cdots\ \ \mathcal{N}_{18}\right]$) of the higher-order 6-node triangular element is obtained. Note that the FSDT is presented by five different field variables (u_x^0, u_y^0, u_z^0, ψ_x,ψ_y) and therefore, there will be a total of $5\times18=90$ DOFs per element (please see Fig. 2). Considering the proposed element, the vector of the displacement field is approximated as

$$U_0 = \overline{\mathcal{N}}\mathbf{q}_0 \tag{79}$$

$$\overline{\mathcal{N}} = \begin{bmatrix} \mathcal{N}_1 & 0 & 0 & 0 & 0 & & \mathcal{N}_{18} & 0 & 0 & 0 & 0 \\ 0 & \mathcal{N}_1 & 0 & 0 & 0 & & 0 & \mathcal{N}_{18} & 0 & 0 & 0 \\ 0 & 0 & \mathcal{N}_1 & 0 & 0 & \ldots & 0 & 0 & \mathcal{N}_{18} & 0 & 0 \\ 0 & 0 & 0 & \mathcal{N}_1 & 0 & & 0 & 0 & 0 & \mathcal{N}_{18} & 0 \\ 0 & 0 & 0 & 0 & \mathcal{N}_1 & & 0 & 0 & 0 & 0 & \mathcal{N}_{18} \end{bmatrix} = \begin{bmatrix} \overline{\mathbf{N}}_e\otimes\mathbf{e}_1 \\ \overline{\mathbf{N}}_e\otimes\mathbf{e}_2 \\ \overline{\mathbf{N}}_e\otimes\mathbf{e}_3 \\ \overline{\mathbf{N}}_e\otimes\mathbf{e}_4 \\ \overline{\mathbf{N}}_e\otimes\mathbf{e}_5 \end{bmatrix} \tag{80}$$

with $\mathbf{q}_0$ as the vector of unknown nodal values (with subscript 0 refering to the plate model). By substituting Eq. (79) into (34), (37) and (55), the vectors of strain and strain gradient are approximated as

$$\varepsilon = \left(\mathbf{P}_1\overline{\mathbf{B}}_e + \frac{1}{2}\mathbf{P}_2\overline{\mathbf{B}}_e^n\right)\mathbf{q}_0,\ \boldsymbol{\kappa} = \left(\mathbf{P}_3\overline{\mathbf{B}}_s + \frac{1}{2}\mathbf{P}_4\overline{\mathbf{B}}_s^n\right)\mathbf{q}_0\ \delta\varepsilon = \left(\mathbf{P}_1\overline{\mathbf{B}}_e + \mathbf{P}_2\overline{\mathbf{B}}_e^n\right)\delta\mathbf{q}_0,\ \delta\boldsymbol{\kappa} = \left(\mathbf{P}_3\overline{\mathbf{B}}_s + \mathbf{P}_4\overline{\mathbf{B}}_s^n\right)\delta\mathbf{q}_0 \tag{81}$$

with the following strain and strain gradient matrices

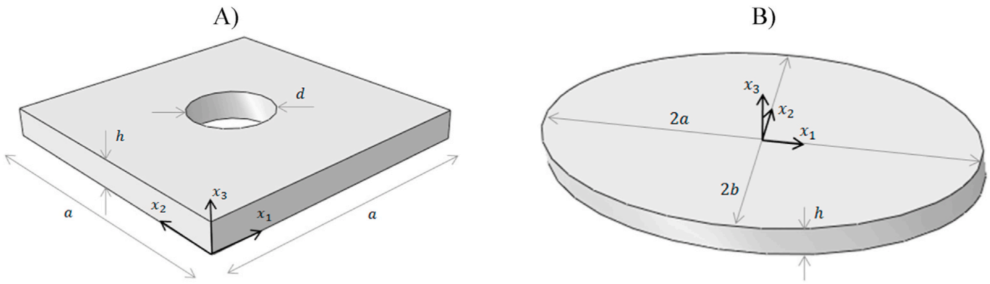

Fig. 3. Schematic view and geometrical parameters for A) a square microplate with a circular hole and B) an elliptical microplate.

$$\overline{\mathbf{B}}_e = \overline{\mathbf{E}}_e\overline{\mathcal{N}},\ \overline{\mathbf{B}}_s = \overline{\mathbf{E}}_s\overline{\mathcal{N}},\ \overline{\mathbf{B}}_e^n = \overline{\mathbf{D}}_1\mathbf{q}_0\overline{\mathbf{D}}_2 + \overline{\mathbf{D}}_2\mathbf{q}_0\overline{\mathbf{D}}_1,\ \overline{\mathbf{B}}_s^n = \overline{\mathbf{M}}_1\mathbf{q}_0\overline{\mathbf{M}}_2 + \overline{\mathbf{M}}_2\mathbf{q}_0\overline{\mathbf{M}}_1 \tag{82}$$

in which the following matrices are used for the nonlinear operators

$$\overline{\mathbf{D}}_i = \overline{\mathbf{G}}_i\overline{\mathcal{N}},\ \overline{\mathbf{M}}_i = \overline{\mathbf{Q}}_i\overline{\mathcal{N}},\ (i = 1, 2) \tag{83}$$

Now, the strain energy is simplified by substituting Eq. (81) into (53) giving

$$\delta\mathscr{F}_e = \delta\mathbf{q}_0^{\mathrm{T}}\overline{\mathbf{K}}\mathbf{q}_0 \tag{84}$$

where the stiffness matrix $\overline{\mathbf{K}}$ is defined as

$$\overline{\mathbf{K}} = \overline{\mathbf{K}}_l + \frac{1}{2}\overline{\mathbf{K}}_{nl} + \frac{1}{3}\overline{\mathbf{K}}_{nl}^* \tag{85}$$

with

$$\overline{\mathbf{K}}_l = \int_A \left(\overline{\mathbf{B}}_e^{\mathrm{T}}\widetilde{\mathcal{C}}_1\overline{\mathbf{B}}_e + \overline{\mathbf{B}}_s^{\mathrm{T}}\widetilde{\mathcal{A}}_1\overline{\mathbf{B}}_s\right)dA,\ \overline{\mathbf{K}}_{nl} = \int_A \left(\overline{\mathbf{B}}_e^{\mathrm{T}}\widetilde{\mathcal{C}}_2\overline{\mathbf{B}}_e^n + 2\overline{\mathbf{B}}_e^{n\mathrm{T}}\widetilde{\mathcal{C}}_3\overline{\mathbf{B}}_e + \overline{\mathbf{B}}_s^{\mathrm{T}}\widetilde{\mathcal{A}}_2\overline{\mathbf{B}}_s^n + 2\overline{\mathbf{B}}_s^{n\mathrm{T}}\widetilde{\mathcal{A}}_3\overline{\mathbf{B}}_s\right)dA\ \overline{\mathbf{K}}_{nl}^* = \frac{3}{2}\int_A \left(\overline{\mathbf{B}}_e^{n\mathrm{T}}\widetilde{\mathcal{C}}_4\overline{\mathbf{B}}_e^n + \overline{\mathbf{B}}_s^{n\mathrm{T}}\widetilde{\mathcal{A}}_4\overline{\mathbf{B}}_s^n\right)dA \tag{86}$$

in which the following material coefficients are considered:

$$\begin{aligned}\widetilde{\mathcal{C}}_1 = \int_{-h/2}^{h/2} \mathbf{P}_1^{\mathrm{T}}\mathcal{C}\mathbf{P}_1\,dz,\ \widetilde{\mathcal{C}}_2 = \int_{-h/2}^{h/2} \mathbf{P}_1^{\mathrm{T}}\mathcal{C}\mathbf{P}_2\,dz,\ \widetilde{\mathcal{C}}_3 = \int_{-h/2}^{h/2} \mathbf{P}_2^{\mathrm{T}}\mathcal{C}\mathbf{P}_1\,dz,\ \widetilde{\mathcal{C}}_4 \\ = \int_{-h/2}^{h/2} \mathbf{P}_2^{\mathrm{T}}\mathcal{C}\mathbf{P}_2\,dz\widetilde{\mathcal{A}}_1 = \int_{-h/2}^{h/2} \mathbf{P}_3^{\mathrm{T}}\mathcal{A}\mathbf{P}_3\,dz\ ,\ \widetilde{\mathcal{A}}_2 \\ = \int_{-h/2}^{h/2} \mathbf{P}_3^{\mathrm{T}}\mathcal{A}\mathbf{P}_4\,dz,\ \widetilde{\mathcal{A}}_3 = \int_{-h/2}^{h/2} \mathbf{P}_4^{\mathrm{T}}\mathcal{A}\mathbf{P}_3\,dz,\ \widetilde{\mathcal{A}}_4 \\ = \int_{-h/2}^{h/2} \mathbf{P}_4^{\mathrm{T}}\mathcal{A}\mathbf{P}_4\,dz\ ,\end{aligned} \tag{87}$$

Moreover, by considering Eq. (33) and substituting Eq. (79) into (56), the variation of the work done by the external forces is given as

$$\delta W_e = \delta\mathbf{q}_0^{\mathrm{T}}\int_V \overline{\mathcal{N}}^{\mathrm{T}}\mathbf{P}_0^{\mathrm{T}}\mathbf{f}\,dzdA + \delta\mathbf{q}_0^{\mathrm{T}}\int_A \overline{\mathcal{N}}^{\mathrm{T}}\mathbf{p}\,dA \tag{88}$$

and can be simplified to

$$\delta W_e = \delta\mathbf{q}_0^{\mathrm{T}}\overline{\mathbf{F}} \tag{89}$$

with

$$\overline{\mathbf{F}} = \int_A \overline{\mathcal{N}}^{\mathrm{T}}\widetilde{\mathbf{f}}\,dA + \int_A \overline{\mathcal{N}}^{\mathrm{T}}\mathbf{p}\,dA \tag{90}$$

$$\widetilde{\mathbf{f}} = \int_{-h/2}^{h/2} \mathbf{P}_0^{\mathrm{T}}\mathbf{f}\,dz \tag{91}$$

Finally, substituting Eqs. (89) and (84) into Eq. (52) gives the final FE equation system via an appropriate assembly procedure for the corresponding global stiffness matrix, displacement vector and force vector in the standard form (including the geometric nonlinearities according to Eqs. (85)–(86), i.e., the dependency of $\overline{\mathbb{K}}$ on q_0)

$$\overline{\mathbb{K}}q_0 + \overline{\mathbb{F}} = 0 \tag{92}$$

7. Results and discussions

The nonlinear FE formulations of the SGT following the 3D theory and the FSDT were presented in the previous sections for the static bending. For numerical integration, the Gaussian quadrature has been employed in this study to evaluate the stiffness matrices and force vectors: seven and eleven Gauss points for the FSDT and 3D problems, respectively. The well-known Newton–Raphson iteration method is utilized to solve the nonlinear finite element equation system.

In this section, two different structures, a square plate with a circular hole and an elliptical plate as shown in Fig. 3, are considered to examine the differences between the models within the regime of geometric nonlinearity. Poisson's ratio is fixed to $\nu = 0.38$.

The numerical examples will be presented for the constitutively simplified version of the SGT, i.e., the MSGT, and the MCST for comparison. For the MSGT, the following assumptions for the SGT material parameters are adopted:

Table 1
Comparison of the linear deflection ($10Eh^3u_z^{max}/qa^4$) of the SSSS square microplate based on the MCST.

l/h	$a/h = 20$ (moderately thin)			$a/h = 10$ (moderately thick)			$a/h = 5$ (thick)		
	3D model	Plate model	Thai et al. (Thai and Choi, 2013)	3D model	Plate model	Thai et al. (Thai and Choi, 2013)	3D model	Plate model	Thai et al. (Thai and Choi, 2013)
0	0.422	0.421	0.423	0.446	0.440	0.442	0.546	0.512	0.515
0.2	0.363	0.367	0.368	0.377	0.383	0.384	0.437	0.446	0.448
0.4	0.260	0.265	0.266	0.270	0.276	0.277	0.314	0.324	0.325
0.6	0.178	0.178	0.178	0.186	0.191	0.191	0.228	0.226	0.227
0.8	0.124	0.123	0.123	0.132	0.134	0.134	0.173	0.162	0.163
1	0.090	0.091	0.091	0.098	0.0972	0.0972	0.141	0.123	0.123

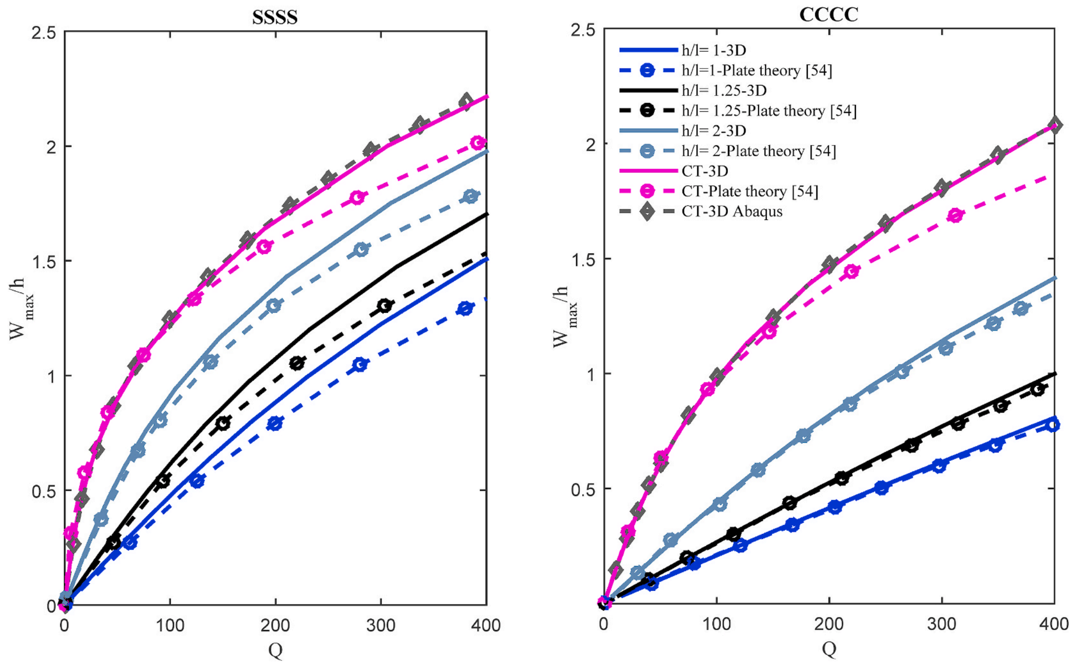

Fig. 4. Comparison of the nonlinear bending responses of the square plate following the MSGT ($a/h = 12$).

Table 2
Comparison of the nondimensional maximum deflection $(10Eh^3u_z^{max}(1-\nu^2)/12q)$ of thin elliptical plates within the classical theory of elasticity ($\nu = 0.3$).

b/a	Ref. (Zhang, 2013)	Present study (FSDT)	Present study (3D)
1	0.156	0.156	0.154
1.2	0.214	0.214	0.212
1.4	0.26	0.260	0.257
1.6	0.295	0.295	0.292
2	0.339	0.339	0.336
3	0.384	0.383	0.38
4	0.399	0.399	0.395
5	0.405	0.405	0.401

$$a_1 = \mu\left(l_2^2 - \frac{4}{15}l_1^2\right),\ a_2 = \mu\left(l_0^2 - \frac{1}{15}l_1^2 - \frac{1}{2}l_2^2\right),\ a_3 = -\mu\left(\frac{4}{15}l_1^2 + \frac{1}{2}l_2^2\right)\ a_4 = \mu\left(\frac{1}{3}l_1^2 + l_2^2\right),\ a_5 = \mu\left(\frac{2}{3}l_1^2 - l_2^2\right) \tag{93}$$

in which $l_0,\ l_1, l_2$ present the material length scales for the MSGT. The results will be presented for $l_0 = l_1 = l_2 = l$. Besides, by letting $l_1 = l_0 = 0$ and $l_2 = l$ one obtains the corresponding results for the MCST. Note that letting $l_0, = l_1 = l_2 = 0$ leads to the corresponding classical theory (CT) of elasticity for both the FSDT and 3D model.

In this study, both clamped (C) and simply supported (S) boundaries are considered. The corresponding mathematical relations for the 3D theory are the following:

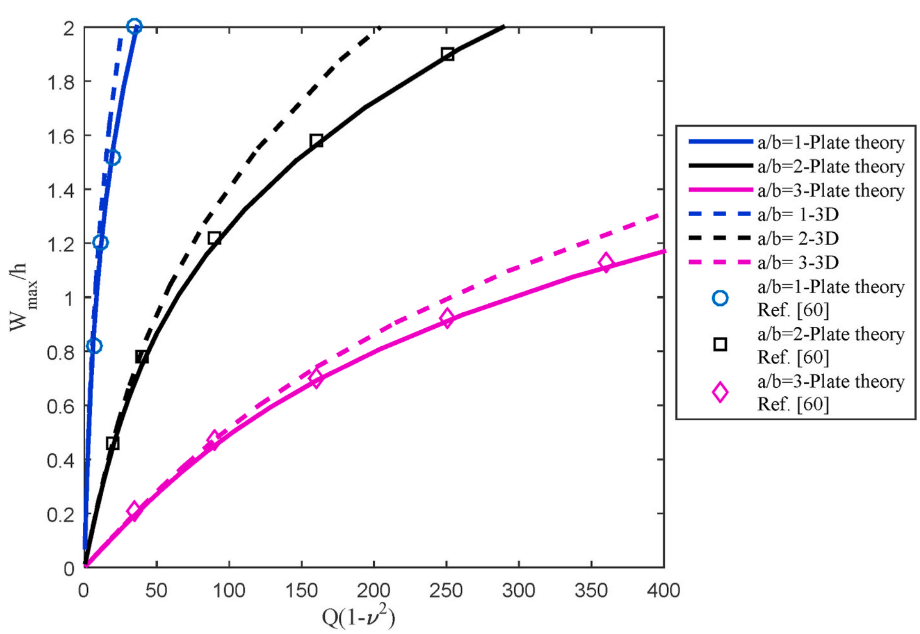

Fig. 5. Comparison of the nonlinear bending responses of the thin square plate following the classical theory of elasticity ($\nu = 0.3$).

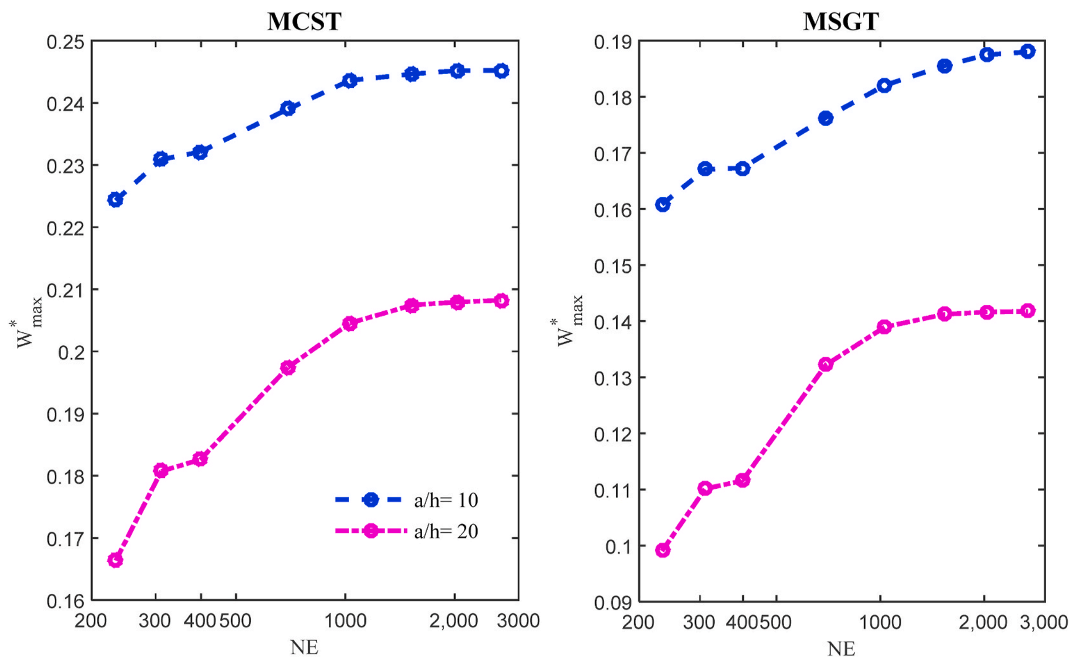

Fig. 6. Convergence study for the nonlinear non-dimensional maximum deflection ($W^*_{max} = 100Eh^3u_z^{max}/qa^4$) of the fully clamped square plate with a circular hole under the 3D model ($h/l = 1.5, d/a = 0.2,\ Q = 300$).

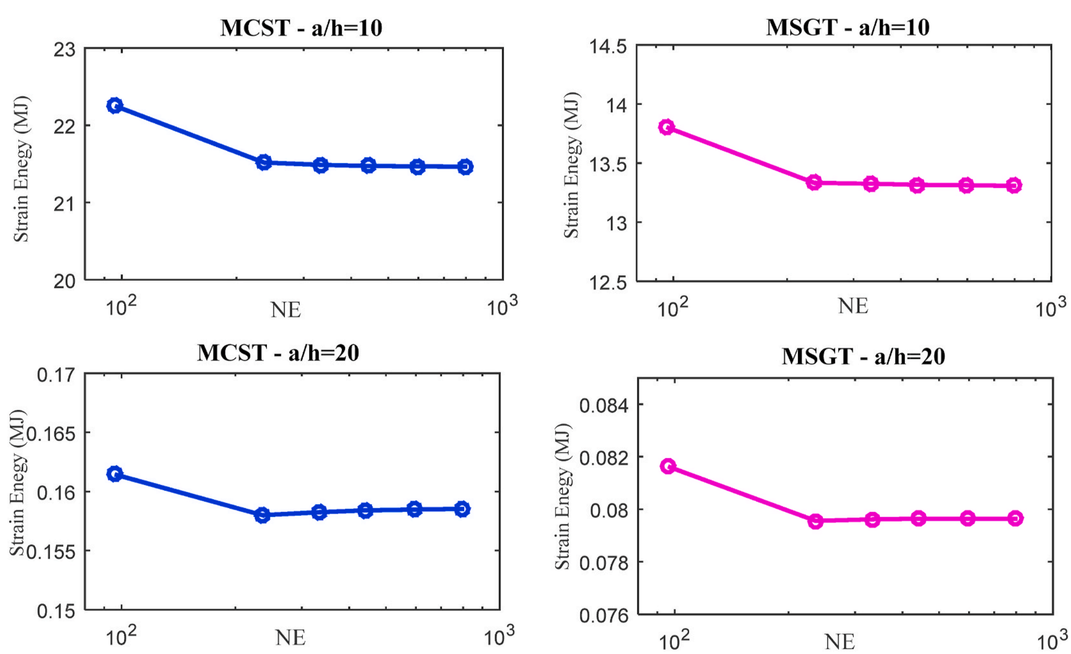

Fig. 7. Convergence study of the total strain energy for the fully clamped square microplate with a circular hole based on the FSDT ($h/l = 1.5, d/a = 0.2,\ Q = 400$).

$$\text{Clamped}: \quad u_n = u_t = u_z = \frac{\partial u_i}{\partial n} = \frac{\partial u_i}{\partial t} = \frac{\partial u_i}{\partial z} = 0, \quad (i = x, y, z) \quad \text{Simply supported}: \quad u_t = u_z = \frac{\partial u_i}{\partial t} = 0, \quad (i = x, y, z) \tag{94}$$

with

$$u_n = n_x u_x + n_y u_y,\ u_t = -n_y u_x + n_x u_y,\ \frac{\partial u_i}{\partial n} = n_x \frac{\partial u_i}{\partial x} + n_y \frac{\partial u_i}{\partial y},\ \frac{\partial u_i}{\partial t} = -n_y \frac{\partial u_i}{\partial x} + n_x \frac{\partial u_i}{\partial y}, \quad (i = x, y, z) \tag{95}$$

For the plate model, the following conditions are imposed:

$$\text{Clamped}:\begin{cases} u_n=u_t=u_z^0=\Psi_n=\Psi_t=0, \\ \dfrac{\partial u_i^0}{\partial n}=\dfrac{\partial u_i^0}{\partial t}=\dfrac{\partial \psi_j}{\partial n}=\dfrac{\partial \psi_j}{\partial t}=0, \end{cases} (i=x,y,z) \text{ and } (j=x,y) \text{ Simply supported}: \begin{cases} u_n=u_t=u_z^0=\Psi_t=0, \\ \dfrac{\partial u_i^0}{\partial t}=\dfrac{\partial \psi_j}{\partial t}=0, \end{cases} (i=x,y,z) \text{ and } (j=x,y) \tag{96}$$

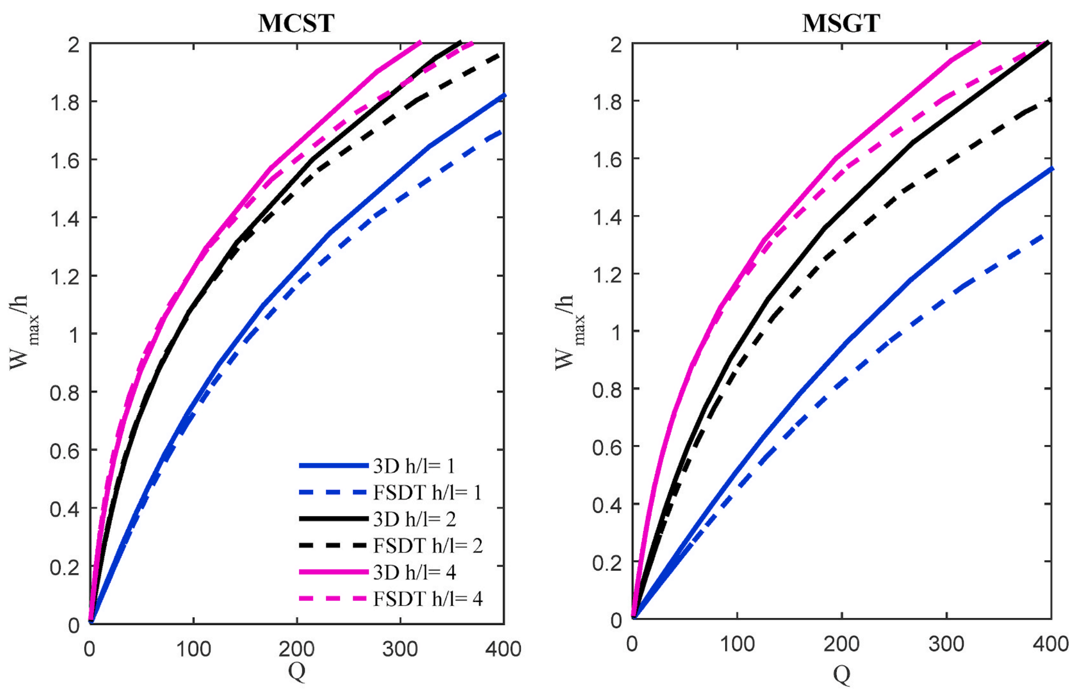

Fig. 8. The impacts of the thickness-to-length-scale ratio on the nonlinear bending of a square plate with a circular hole ($a/h = 10, d/a = 0.2$, SSSS).

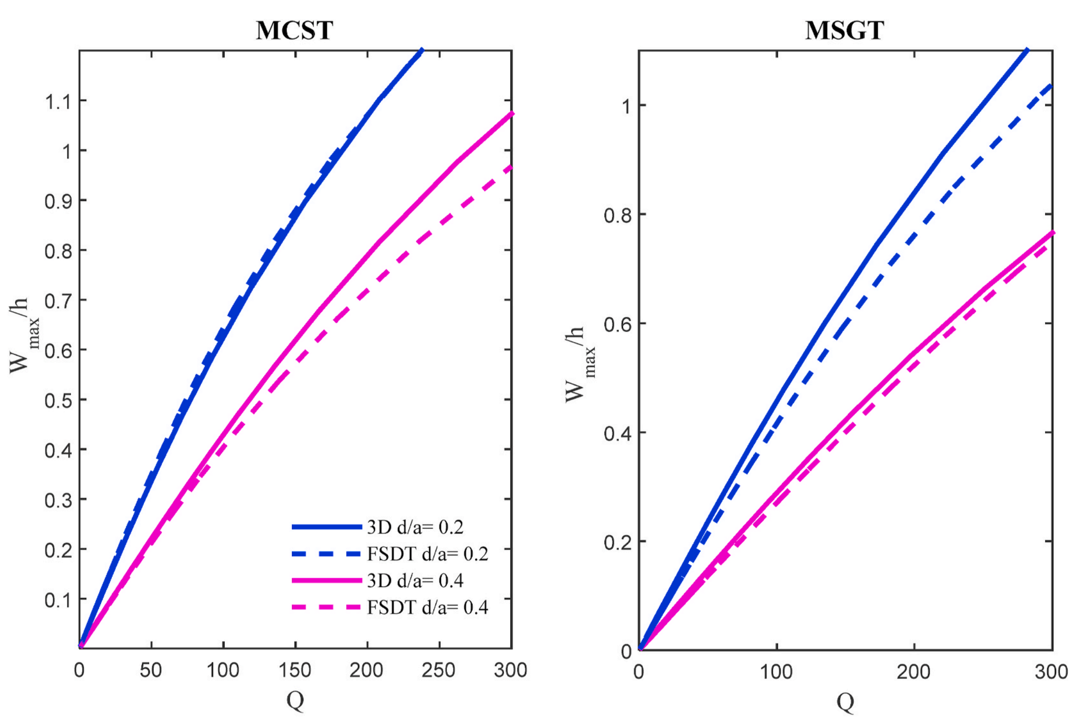

Fig. 9. The effects of the hole-diameter-to-length ratio on the nonlinear bending response of a fully clamped square plate with a circular hole ($h/l = 2, a/h = 10$).

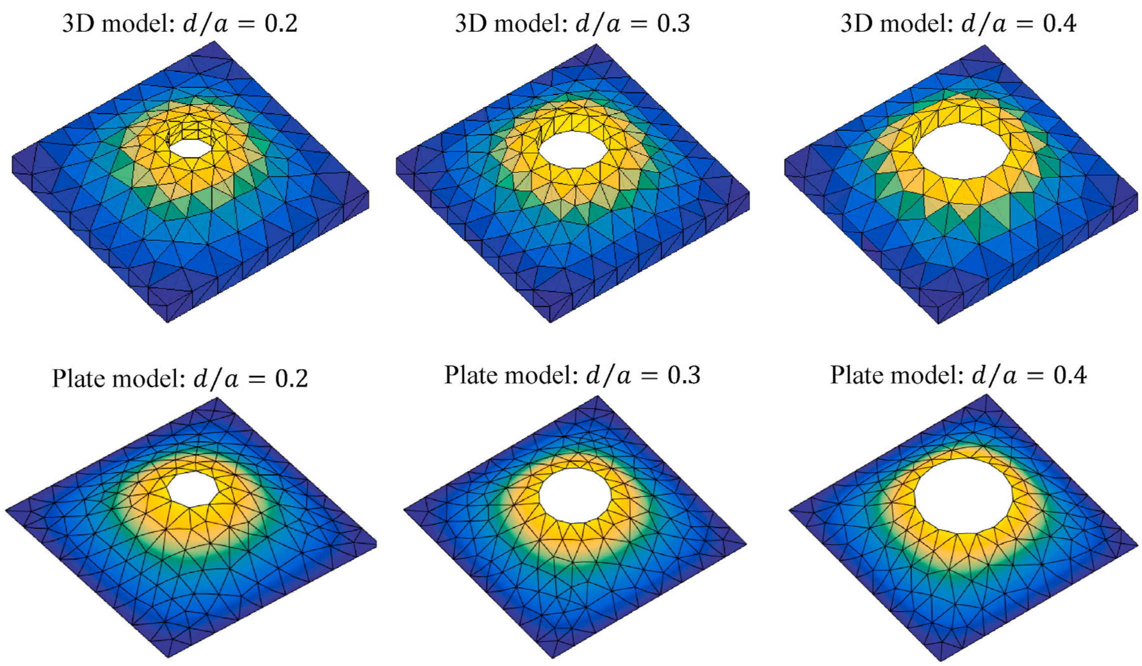

Fig. 10. Deformation shapes of the clamped square microplates under the MSGT ($a/h = 10, h/l = 2$).

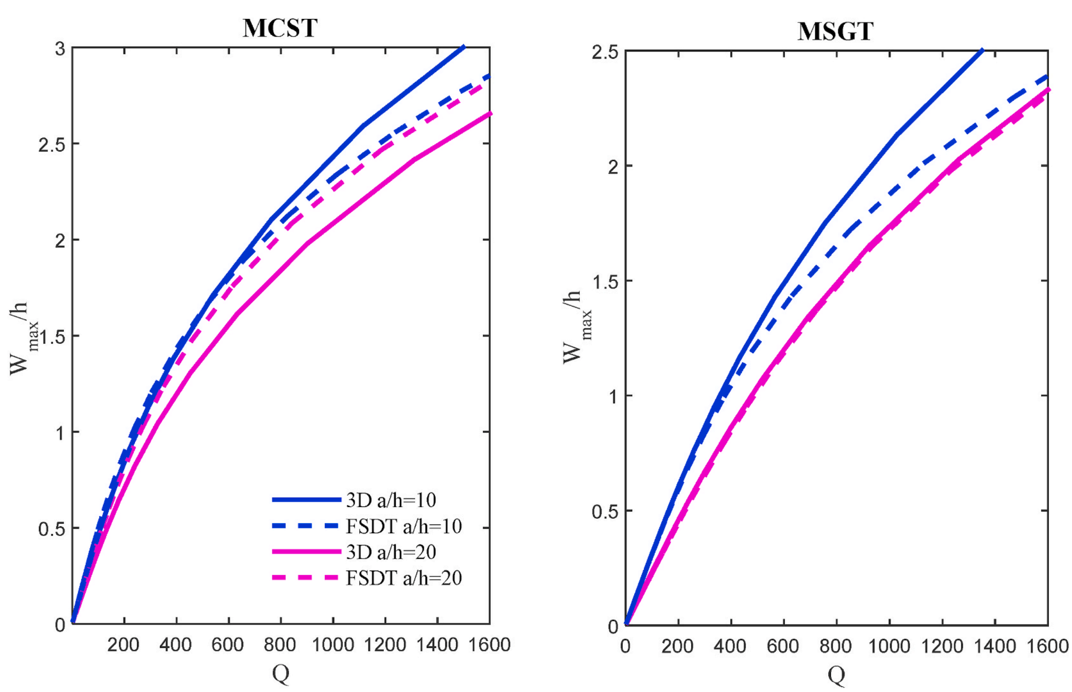

Fig. 11. The effects of the length-to-thickness ratio on the nonlinear bending response of a fully clamped plate with a hole ($h/l = 1.5, d/a = 0.2$).

with

$$u_n = n_x u_x^0 + n_y u_y^0,\ u_t = -n_y u_x^0 + n_x u_y^0,\ \Psi_n = n_x \psi_x + n_y \psi_y,\ \Psi_t = -n_y \psi_x + n_x \psi_y,\ \frac{\partial u_i^0}{\partial n} = n_x \frac{\partial u_i^0}{\partial x} + n_y \frac{\partial u_i^0}{\partial y},\ \frac{\partial u_i^0}{\partial t} = -n_y \frac{\partial u_i^0}{\partial x} + n_x \frac{\partial u_i^0}{\partial y},\ (i=x,y,z)\ \frac{\partial \psi_j}{\partial n} = n_x \frac{\partial \psi_j}{\partial x} + n_y \frac{\partial \psi_j}{\partial y},\ \frac{\partial \psi_j}{\partial t} = -n_y \frac{\partial \psi_j}{\partial x} + n_x \frac{\partial \psi_j}{\partial y},\ (j=x,y) \tag{97}$$

In the above equations, $\mathbf{n} = [n_x n_y]$ expresses the outward unit normal vector of the boundary curve.

7.1. Comparisons to earlier studies

The proposed models are validated through four different comparative studies. First, the non-dimensional linear deflections of the square plate are presented in Table 1 and compared for different thickness ratios with the results of Thai et al. (Thai and Choi, 2013) following the MCST. Generally, a good agreement between all of the results is observed, but differences between the plate models and the 3D model increase for small length-to-thickness ratios (thick plates). For

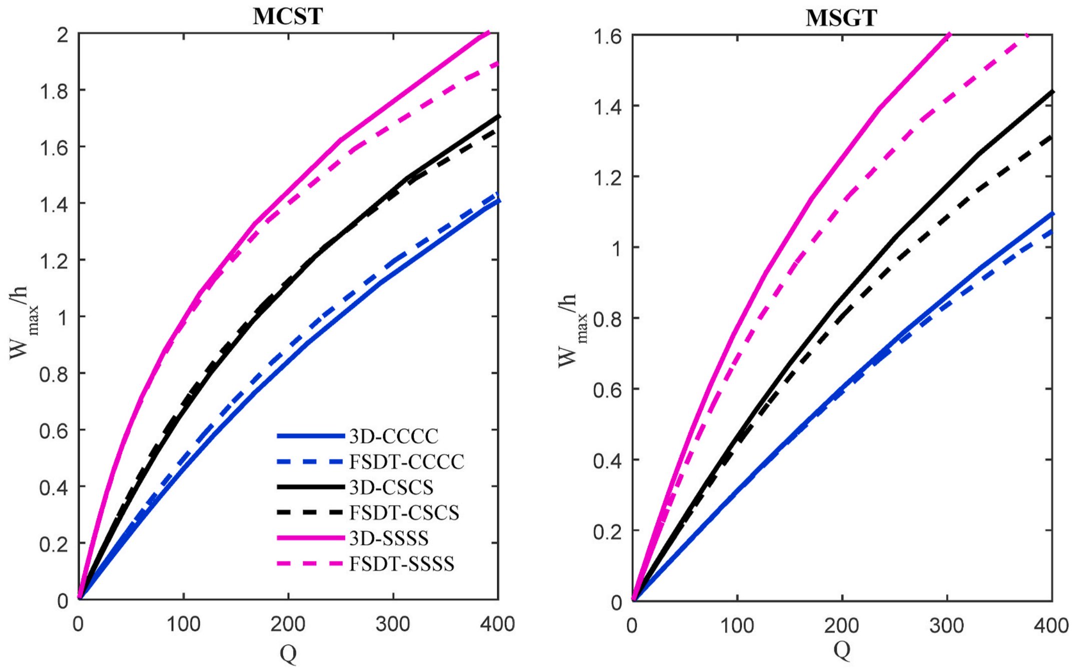

Fig. 12. The effects of the edge supports on the nonlinear bending of a square plate with a circular hole ($a/h = 10,\ d/a = 0.2, h/l = 1.5$).

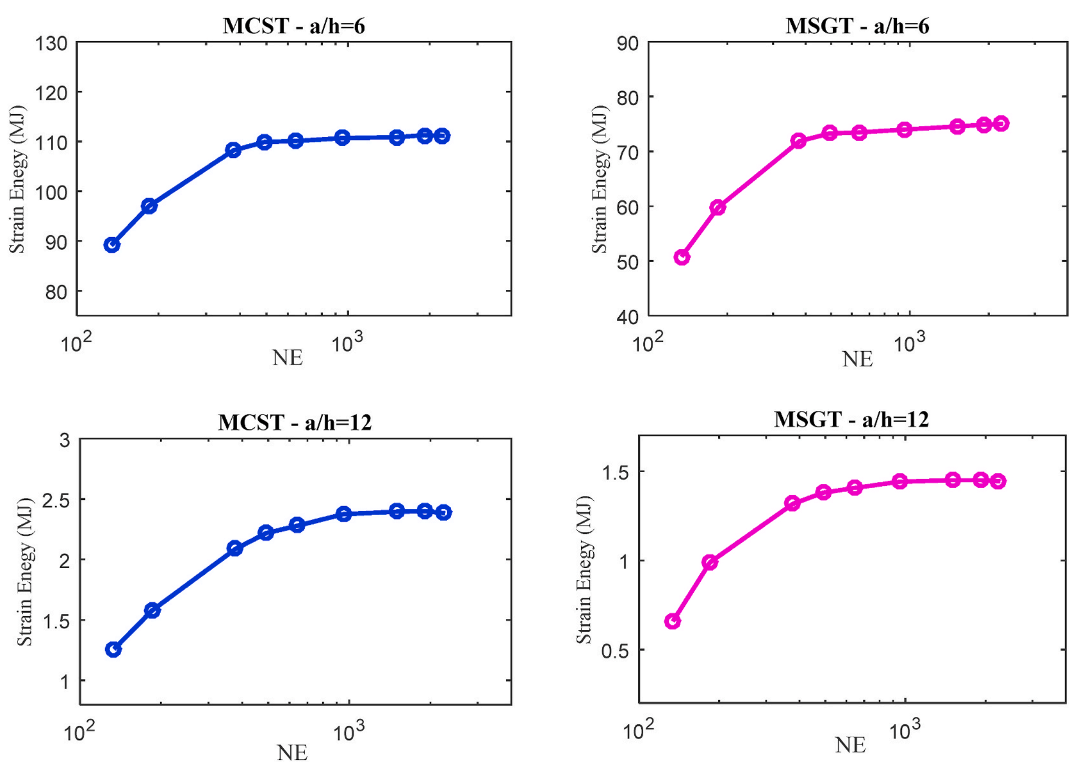

Fig. 13. Convergence study of the total strain energy for the clamped elliptical plate based on the 3D model ($h/l = 1.5, a/b = 2,\ Q = 300$).

moderately thin and thin plates, say for $a/h \geq 20$, the differences between models in linear regime are practically negligible.

Second, a comparison of the nonlinear bending responses of the square plate is presented in Fig. 4 for the MSGT. The results of the 3D model are compared with those of Ref (Ansari et al., 2016b). presented based on the FSDT. In the case of the classical elasticity theory, results obtained with the FE software Abaqus are also included. Note that our results based on the triangular FSDT plate element match with those of Ref (Ansari et al., 2016b). and are hence omitted in the plots. In general, the results show that the plate model and the 3D model differ from each other for the higher values of the loading, especially for the simply supported plate.

Note that for the comparison studies, the boundary conditions are different from Eqs. (94) and (96) and considered based on the relations defined in Ref (Ansari et al., 2016b). as follows:

3D model:

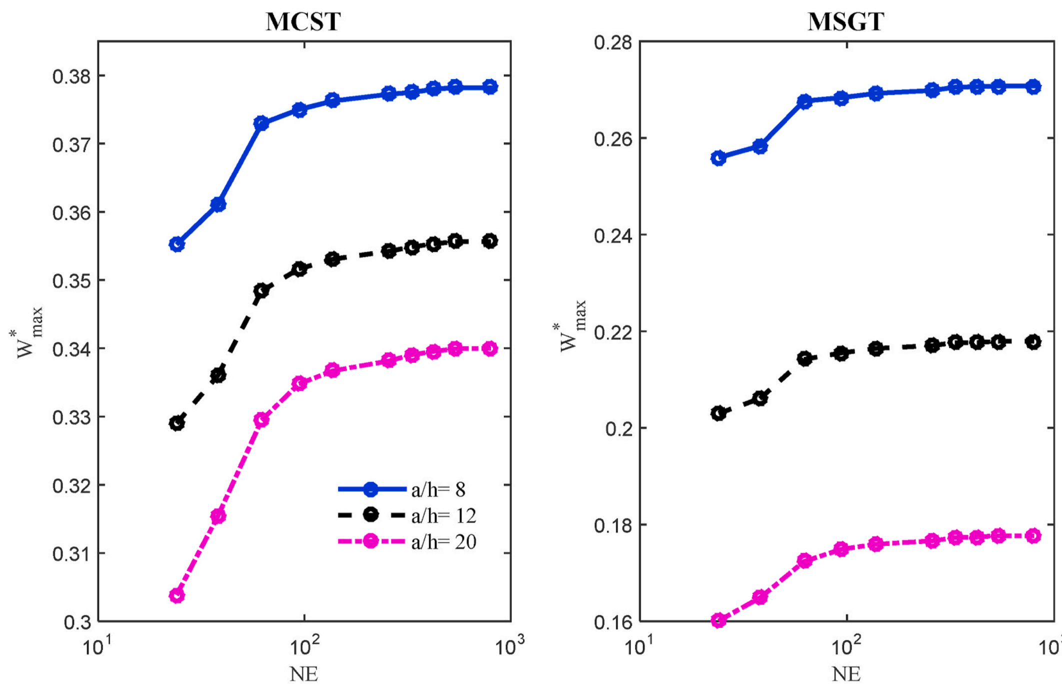

Fig. 14. Convergence study for the nonlinear non-dimensional maximum deflection ($W^*_{max} = 100Eh^3u_z^{max}/qa^4$) of a clamped elliptical plate based on the FSDT ($h/l = 1.5, a/b = 2, Q = 150$).

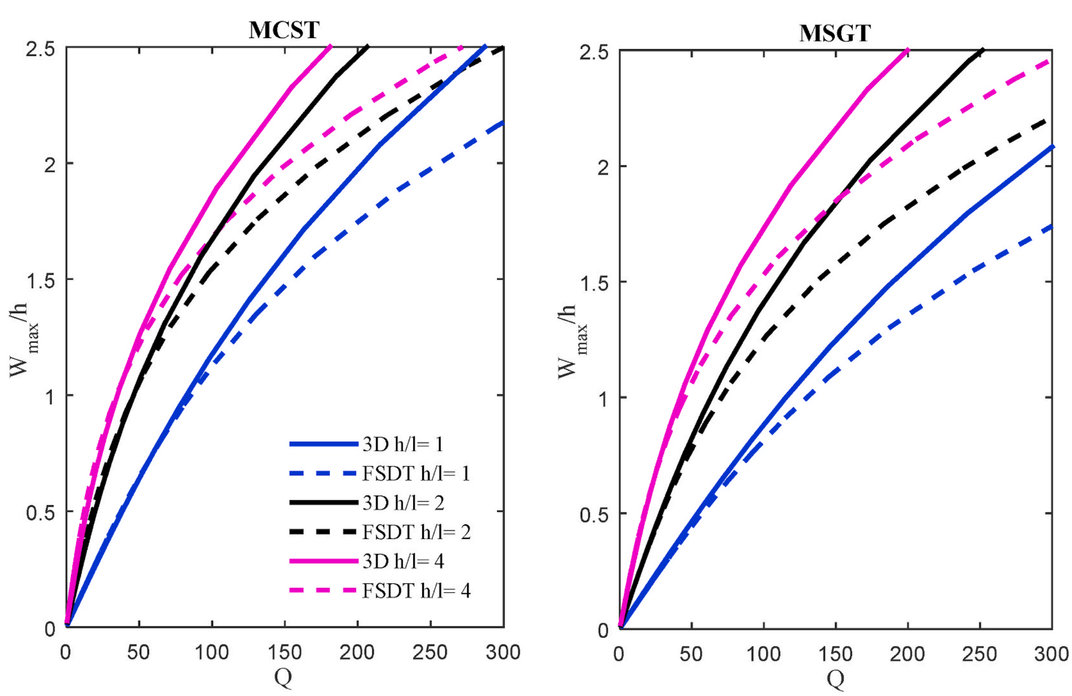

Fig. 15. The effects of thickness-to-length-scale ratio on the nonlinear bending response of a clamped elliptical plate ($a/b = 1.6, a/h = 6$).

Table 3
Variations of the nonlinear maximum nondimensinal deflection of a clamped elliptical plate ($a/b = 1.6, a/h = 6$).

Model	Q	MCST			MSGT		
		$\frac{h}{l} = 1$	$\frac{h}{l} = 2$	$\frac{h}{l} = 4$	$\frac{h}{l} = 1$	$\frac{h}{l} = 2$	$\frac{h}{l} = 4$
3D elasticity	40	0.519	0.900	1.092	0.374	0.681	0.969
	80	0.975	1.461	1.650	0.722	1.201	1.527
	120	1.362	1.867	2.047	1.035	1.600	1.927
	160	1.692	2.194	2.367	1.315	1.925	2.247
	200	1.979	2.472	2.638	1.564	2.200	2.518
Plate model	40	0.529	0.914	1.088	0.358	0.654	0.932
	80	0.952	1.378	1.527	0.676	1.089	1.378
	120	1.277	1.687	1.818	0.944	1.396	1.675
	160	1.537	1.924	2.043	1.168	1.633	1.903
	200	1.753	2.119	2.229	1.360	1.829	2.091

$$\text{Clamped}: \quad u_n = u_t = u_z = \frac{\partial u_z}{\partial n} = 0, \ \text{Simply supported}: \quad u_t = u_z = \frac{\partial u_z}{\partial t} = 0, \tag{98}$$

Plate model:

$$\text{Clamped}: \quad u_n = u_t = u_z^0 = \Psi_n = \frac{\partial u_z^0}{\partial n} = \frac{\partial \Psi_t}{\partial n} = 0, \ \text{Simply}-\text{supported} : \quad u_n = u_t = u_z^0 = \Psi_t = \frac{\partial \Psi_n}{\partial n} = 0, \tag{99}$$

As other comparisons, the linear and nonlinear bending responses of the clamped elliptical thin plate within the classical theory of elasticity are compared with the results provided by Zhang (2013) in Table 2 and Fig. 5, respectively. As can be seen in Table 2 for the linear analysis of thin plates there is practically no difference between the results given by

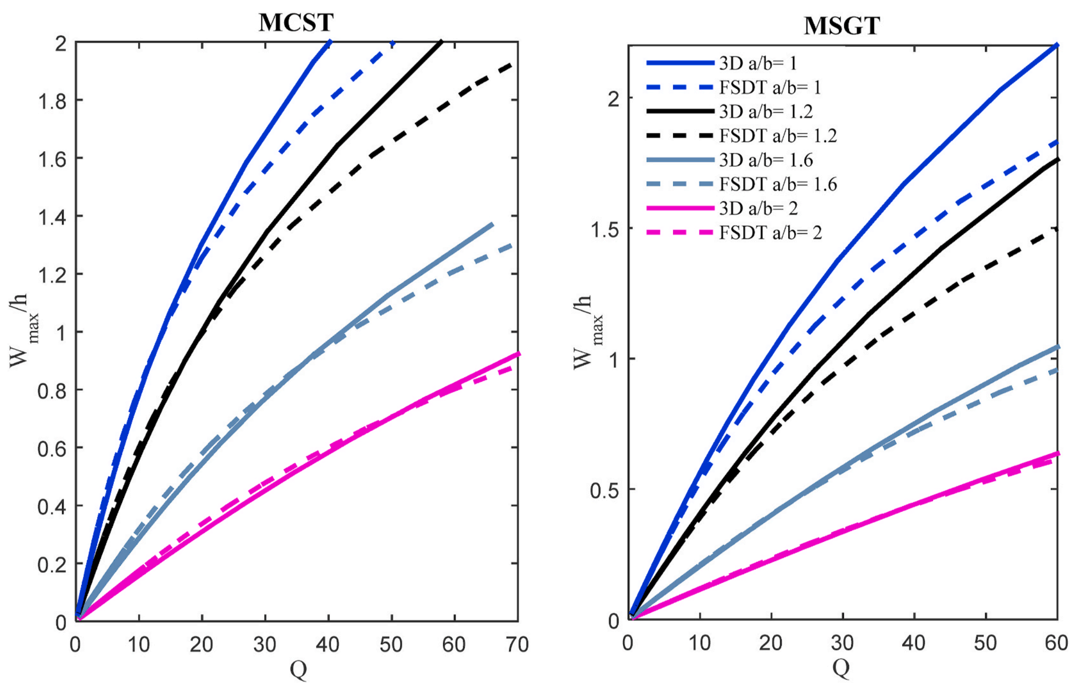

Fig. 16. The effects of the aspect ratio on the nonlinear bending response for a clamped elliptical plate ($h/l = 2, a/h = 5$).

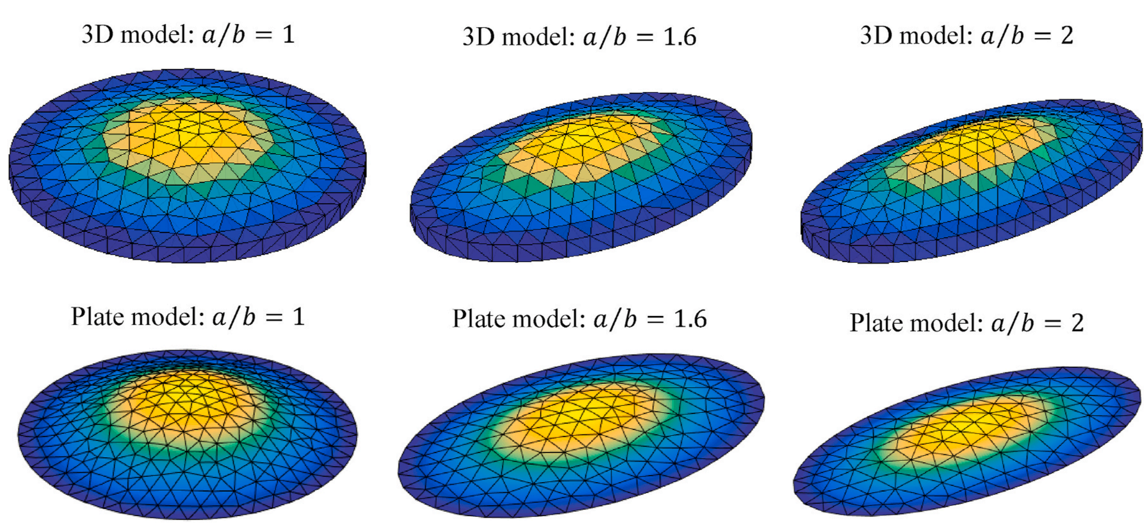

Fig. 17. Deformation shapes of the clamped elliptical microplates under the MSGT ($a/h = 10, h/l = 2$).

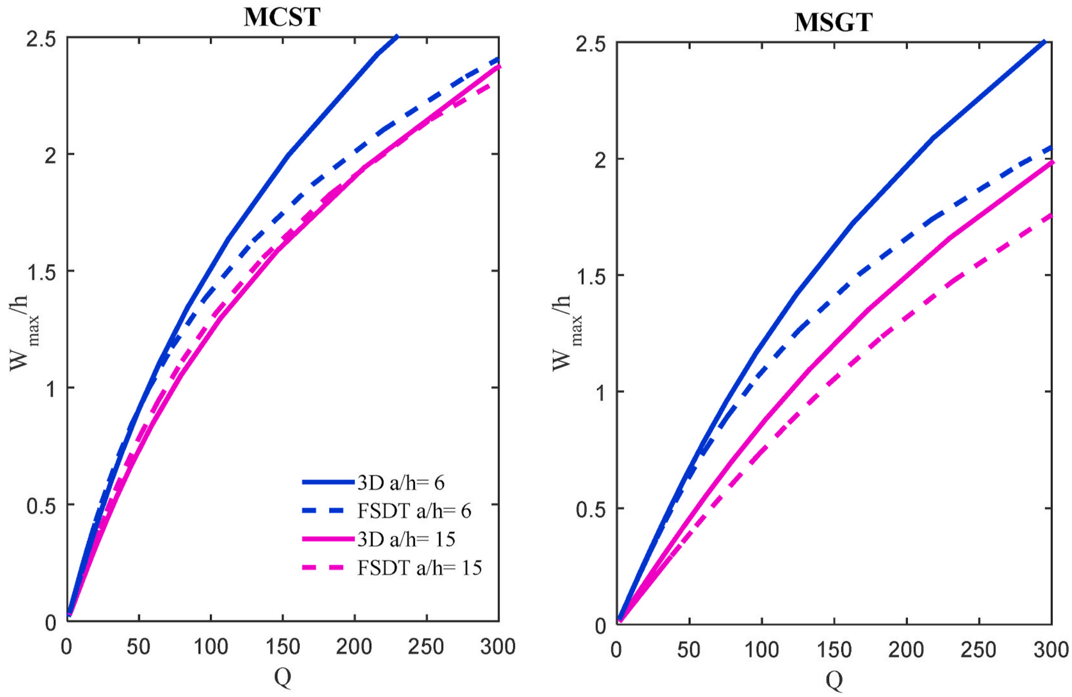

Fig. 18. The effects of the diameter-to-thickness ratio on the nonlinear bending response of a clamped elliptical plate ($a/b = 1.6$, $h/l = 1.5$).

different models. Within the nonlinear regime for elliptical thin plates, instead, the difference between the 3D model and the plate models becomes remarkable, as illustrated in Fig. 5.

In what follows, various parametric studies are provided for the two case studies demonstrated in Fig. 3 to highlight the differences between the 3D model and the FSDT plate model. The variations of the dimensionless deflection (W_{max}/h) versus the load parameter ($Q = qEh^4/a^4$) are illustrated as the nonlinear bending response where $W_{max} = u_z^{max}$ is the maximum deflection and q is the uniformly distributed load.

7.2. Square plate with a circular hole

The numerical reliability and efficiency of the proposed elements are examined in Figs. 6 and 7 for the 3D and plate models, respectively, by plotting the maximum deflection or the strain energy versus the number of elements (NE) for the MCST (left) and MSGT (right) showing good convergence for both cases. The convergence studies were checked for both maximum deflection and the strain energy but only one for each case was reported since the results are very similar. It should be noticed that since neither the hexahedral solid element nor the plane triangular element are fully C^1-continuous (i.e., conforming), the approximate strain energy or the displacement field might approach the corresponding exact value from above as well, as it happens in Fig. 7.

The nonlinear bending responses for a fully simply supported square plate are demonstrated in Fig. 8 for different thickness-to-length-scale ratios for the MCST and MSGT to highlight the differences between the 3D and plate models. The effect of the gradient terms becomes evident as well. It is found that by increasing the applied load, the differences get increased and the 3D model predicts larger values for the non-dimensional deflection. The increase of the h/l ratio results in larger deflection values and enhances the impacts of geometric nonlinearity, whereas it makes the difference between the plate model and the 3D model smaller.

Next, the nonlinear bending responses for a square plate with a hole are presented in Fig. 9 for the MCST and MSGT for two different hole diameters. The fully clamped boundary condition is adopted. Different characters are observed for the size-dependent theories: in the case of the MCST, the difference between the 3D and plate models is more considerable for $d/a = 0.4$, whereas the major difference is found for $d/a = 0.2$ for the MSGT. Besides, the deformation shapes of the clamped square microplate based on the 3D and plate models under the MSGT are presented in Fig. 10 for three different cutouts.

Demonstrated in Fig. 11 are the effects of the length-to-thickness ratio (a/h) on the bending responses of the fully clamped plate with a hole following the MCST and MSGT. The results are presented for both the 3D and plate models to highlight the differences. The FSDT is less sensitive to the length-to-thickness ratio than the 3D model. Comparing the results for the MCST and MSGT indicates that the latter one provides a stiffer structural model.

The impacts of boundary conditions on the nonlinear bending responses are demonstrated in Fig. 12 for the square plate. The maximum non-dimensional deflection versus the load parameter is presented for CCCC, CSCS and SSSS edge supports. Note that CSCS implies that the edges at $x = 0, a$ are clamped and the other two sides are simply supported. It can be generally seen that the differences between the 3D theory and the FSDT are more considerable for a fully simply supported structure. The results also reveal that the impact of the terms of geometrical nonlinearity is pronounced for the simply supported boundary conditions.

7.3. Elliptical plate

Some convergence studies for the maximum non-dimensional deflection and strain energy of a clamped elliptical plate for the 3D theory and the FSDT are provided in Figs. 13 and 14, respectively, for three length-to-thickness ratios showing good convergence properties in both cases.

The nonlinear bending responses of a clamped elliptical plate are illustrated in Fig. 15 and Table 3 for various length scales for both the MCST and the MSGT. Remarkable differences are observed between the results provided by the 3D theory and the FSDT. For the MCST, one can see considerable discrepancies for the non-dimensional deflections larger than one ($W_{max}/h > 1$). Similar results are observed for the MSGT as well showing the importance of the Green–Lagrange strain terms in large deformations.

Besides, the effects of the aspect ratio (a/b) on the nonlinear bending responses of the clamped elliptical plate are investigated in Fig. 16. The results are presented for the 3D model and plate models for both the MCST and the MSGT. One can see that the increase in the aspect ratio considerably reduces the non-dimensional maximum deflection. It is figured out that the differences are quite remarkable for circular-type plates and for the same applied load level the discrepancies get essentially decreased for larger aspect ratios. In addition, the deformation shapes of the clamped elliptical microplate by the 3D and plate models under the MSGT are represented in Fig. 17 for three different aspect ratios.

Finally, the impacts of the length-to-thickness ratio (a/h) for the nonlinear bending of the clamped elliptical plate are demonstrated in Fig. 18. It can be seen that in the case of the MCST and based on the FSDT the results for different thickness ratios are close to each other, whereas the 3D model predicts larger differences between the different values of this ratio. On the other hand, profound differences are observed for the 3D and plate models in the case of the MSGT, which shows the importance of the 3D elasticity model in certain circumstances.

8. Conclusion

By considering Mindlin's SGT and based on two structural models – the 3D elasticity theory and the corresponding FSDT – the related FE formulations were presented in order to investigate the geometrically nonlinear bending of plates. For the nonlinear FE formulations of the 3D theory and the FSDT within the SGT, appropriate matrix-vector forms with the nonlinear kinematic relations and linear constitutive laws were defined for tetrahedral and triangular elements, respectively.

In order to examine the differences between these two structural models, various comparative results for nonlinear static bending analysis were reported. It is generally observed that by the increase of the applied load, the differences between the 3D and plate models become more pronounced showing the importance of the Green–Lagrange strain relations. It is also concluded that increasing the thickness-to-length-scale ratio makes the structure relatively softer and increases the impacts of geometrical nonlinearity. A comparison of the nonlinear bending results for different boundary conditions revealed that a fully simply supported structure results in a larger difference between the 3D and plate models than in the case of a fully or partly clamped structure. Studying the effects of the aspect ratio on the nonlinear bending responses of elliptical plates revealed that the discrepancies between the two structural models get decreased by increasing the aspect ratio.

Declaration of competing interest

All authors declare that they do not have any conflict of interest.

References

Ansari, R., Torabi, J., 2016. Nonlocal vibration analysis of circular double-layered graphene sheets resting on an elastic foundation subjected to thermal loading. Acta Mech. Sin. 32 (5), 841–853.
Ansari, R., Gholami, R., Shojaei, M.F., Mohammadi, V., Sahmani, S., 2015a. Bending, buckling and free vibration analysis of size-dependent functionally graded circular/annular microplates based on the modified strain gradient elasticity theory. Eur. J. Mech. Solid. 49, 251–267.
Ansari, R., Shojaei, M.F., Mohammadi, V., Bazdid-Vahdati, M., Rouhi, H., 2015b. Triangular Mindlin microplate element. Comput. Methods Appl. Mech. Eng. 295, 56–76.
Ansari, R., Shojaei, M.F., Gholami, R., 2016a. Size-dependent nonlinear mechanical behavior of third-order shear deformable functionally graded microbeams using the variational differential quadrature method. Compos. Struct. 136, 669–683.
Ansari, R., Shojaei, M.F., Shakouri, A.H., Rouhi, H., 2016b. Nonlinear bending analysis of first-order shear deformable microscale plates using a strain gradient quadrilateral Element. J. Comput. Nonlinear Dynam. 11 (5), 051014.
Balobanov, V., Niiranen, J., 2018. Locking-free variational formulations and isogeometric analysis for the Timoshenko beam models of strain gradient and classical elasticity. Comput. Methods Appl. Mech. Eng. 339, 137–159.
Balobanov, V., Kiendl, J., Khakalo, S., Niiranen, J., 2019. Kirchhoff–Love shells within strain gradient elasticity: weak and strong formulations and an H3-conforming isogeometric implementation. Comput. Methods Appl. Mech. Eng. 344, 837–857.
Barretta, R., Faghidian, S.A., Luciano, R., 2019. Longitudinal vibrations of nano-rods by stress-driven integral elasticity. Mech. Adv. Mater. Struct. 26 (15), 1307–1315.
Dadgar-Rad, F., 2017. Analysis of strain gradient Reissner–Mindlin plates using a C0 four-node quadrilateral element. Int. J. Mech. Sci. 122, 79–94.
dell'Isola, F., Seppecher, P., Spagnuolo, M., Barchiesi, E., Hild, F., Lekszycki, T., et al., 2019. Advances in pantographic structures: design, manufacturing, models, experiments and image analyses. Continuum Mech. Therm. 31 (4), 1231–1282.
Dell'Isola, F., Seppecher, P., Alibert, J.J., Lekszycki, T., Grygoruk, R., Pawlikowski, M., Gołaszewski, M., 2019a. Pantographic metamaterials: an example of mathematically driven design and of its technological challenges. Continuum Mech. Therm. 31 (4), 851–884.
Dell'Isola, F., Seppecher, P., Spagnuolo, M., et al., 2019b. Advances in pantographic structures: design, manufacturing, models, experiments and image analyses. Continuum Mech. Therm. 31 (4), 1231–1282.
Dell'Isola, F., Seppecher, P., Alibert, J.J., Lekszycki, T., Grygoruk, R., Pawlikowski, M., et al., 2019c. Pantographic metamaterials: an example of mathematically driven design and of its technological challenges. Continuum Mech. Therm. 31 (4), 851–884.
Engel, G., Garikipati, K., Hughes, T.J., Larson, M.G., Mazzei, L., Taylor, R.L., 2002. Continuous/discontinuous finite element approximations of fourth-order elliptic problems in structural and continuum mechanics with applications to thin beams and plates, and strain gradient elasticity. Comput. Methods Appl. Mech. Eng. 191 (34), 3669–3750.
Eringen, A.C., 1972. Nonlocal polar elastic continua. Int. J. Eng. Sci. 10 (1), 1–16.
Eringen, A.C., 1983. On differential equations of nonlocal elasticity and solutions of screw dislocation and surface waves. J. Appl. Phys. 54 (9), 4703–4710.
Farahmand, H., Ahmadi, A.R., Arabnejad, S., 2011. Thermal buckling analysis of rectangular microplates using higher continuity p-version finite element method. Thin-Walled Struct. 49 (12), 1584–1591.
Fischer, P., Klassen, M., Mergheim, J., Steinmann, P., Müller, R., 2011. Isogeometric analysis of 2D gradient elasticity. Comput. Mech. 47 (3), 325–334.
Ghayesh, M.H., Amabili, M., Farokhi, H., 2013. Nonlinear forced vibrations of a microbeam based on the strain gradient elasticity theory. Int. J. Eng. Sci. 63, 52–60.
Hosseini, M., Shishesaz, M., Hadi, A., 2019. Thermoelastic analysis of rotating functionally graded micro/nanodisks of variable thickness. Thin-Walled Struct. 134, 508–523.
Javili, A., dell'Isola, F., Steinmann, P., 2013. Geometrically nonlinear higher-gradient elasticity with energetic boundaries. J. Mech. Phys. Solid. 61 (12), 2381–2401.
Kahrobaiyan, M.H., Asghari, M., Rahaeifard, M., Ahmadian, M.T., 2011. A nonlinear strain gradient beam formulation. Int. J. Eng. Sci. 49 (11), 1256–1267.
Ke, L.L., Wang, Y.S., 2011. Size effect on dynamic stability of functionally graded microbeams based on a modified couple stress theory. Compos. Struct. 93 (2), 342–350.
Ke, L.L., Yang, J., Kitipornchai, S., Bradford, M.A., 2012. Bending, buckling and vibration of size-dependent functionally graded annular microplates. Compos. Struct. 94 (11), 3250–3257.
Khakalo, S., Niiranen, J., 2018. Form II of Mindlin's second strain gradient theory of elasticity with a simplification: for materials and structures from nano-to macro-scales. Eur. J. Mech. Solid. 71, 292–319.
Khakalo, S., Niiranen, J., 2019. Lattice structures as thermoelastic strain gradient metamaterials: evidence from full-field simulations and applications to functionally step-wise-graded beams. Compos. B Eng. 177, 107224.
Khakalo, S., Niiranen, J., 2020. Anisotropic strain gradient thermoelasticity for cellular structures: plate models, homogenization and isogeometric analysis. J. Mech. Phys. Solid. 134, 103728.
Khakalo, S., Balobanov, V., Niiranen, J., 2018. Modelling size-dependent bending, buckling and vibrations of 2D triangular lattices by strain gradient elasticity models: applications to sandwich beams and auxetics. Int. J. Eng. Sci. 127, 33–52.
Kwon, Y.R., Lee, B.C., 2017. A mixed element based on Lagrange multiplier method for modified couple stress theory. Comput. Mech. 59 (1), 117–128.
Lam, D.C., Yang, F., Chong, A.C.M., Wang, J., Tong, P., 2003. Experiments and theory in strain gradient elasticity. J. Mech. Phys. Solid. 51 (8), 1477–1508.
Lazopoulos, K.A., Lazopoulos, A.K., 2010. Bending and buckling of thin strain gradient elastic beams. Eur. J. Mech. Solid. 29 (5), 837–843.
Lazopoulos, K.A., Lazopoulos, A.K., 2011. Nonlinear strain gradient elastic thin shallow shells. Eur. J. Mech. Solid. 30 (3), 286–292.
Lestringant, C., Audoly, B., 2020. Asymptotically exact strain-gradient models for nonlinear slender elastic structures: a systematic derivation method. J. Mech. Phys. Solid. 136, 103730.
Mindlin, R.D., 1964. Micro-structure in linear elasticity. Arch. Ration. Mech. Anal. 16 (1), 51–78.
Mindlin, R.D., 1965. Second gradient of strain and surface-tension in linear elasticity. Int. J. Solid Struct. 1 (4), 417–438.
Mindlin, R.D., Tiersten, H.F., 1962. Effects of couple-stresses in linear elasticity. Arch. Ration. Mech. Anal. 11 (1), 415–448.
Mirjavadi, S.S., Forsat, M., Barati, M.R., Abdella, G.M., Afshari, B.M., Hamouda, A.M.S., Rabby, S., 2019. Dynamic response of metal foam FG porous cylindrical micro-shells due to moving loads with strain gradient size-dependency. The European Physical Journal Plus 134 (5), 1–11.
Movassagh, A.A., Mahmoodi, M.J., 2013. A micro-scale modeling of Kirchhoff plate based on modified strain-gradient elasticity theory. Eur. J. Mech. Solid. 40, 50–59.
Nguyen, H.X., Atroshchenko, E., Ngo, T., Nguyen-Xuan, H., Vo, T.P., 2019. Vibration of cracked functionally graded microplates by the strain gradient theory and extended isogeometric analysis. Eng. Struct. 187, 251–266.
Niiranen, J., Khakalo, S., Balobanov, V., Niemi, A.H., 2016. Variational formulation and isogeometric analysis for fourth-order boundary value problems of gradient-elastic

bar and plane strain/stress problems. Comput. Methods Appl. Mech. Eng. 308, 182–211.
Niiranen, J., Kiendl, J., Niemi, A.H., Reali, A., 2017. Isogeometric analysis for sixth-order boundary value problems of gradient-elastic Kirchhoff plates. Comput. Methods Appl. Mech. Eng. 316, 328–348.
Niiranen, J., Balobanov, V., Kiendl, J., Hosseini, S.B., 2019. Variational formulations, model comparisons and numerical methods for Euler–Bernoulli micro-and nano-beam models. Math. Mech. Solid 24 (1), 312–335.
Papanicolopulos, S.A., Zervos, A., Vardoulakis, I., 2009. A three-dimensional C^1 finite element for gradient elasticity. Int. J. Numer. Methods Eng. 77 (10), 1396–1415.
Park, S.K., Gao, X.L., 2006. Bernoulli–Euler beam model based on a modified couple stress theory. J. Micromech. Microeng. 16 (11), 2355.
Ramezani, S., 2012. A shear deformation micro-plate model based on the most general form of strain gradient elasticity. Int. J. Mech. Sci. 57 (1), 34–42.
Romano, G., Barretta, R., 2017. Nonlocal elasticity in nanobeams: the stress-driven integral model. Int. J. Eng. Sci. 115, 14–27.
Schulte, J., Dittmann, M., Eugster, S.R., Hesch, S., Reinicke, T., dell'Isola, F., Hesch, C., 2020. Isogeometric analysis of fiber reinforced composites using Kirchhoff-Love shell elements. Comput. Methods Appl. Mech. Eng. 362, 112845.
Thai, H.T., Choi, D.H., 2013. Size-dependent functionally graded Kirchhoff and Mindlin plate models based on a modified couple stress theory. Compos. Struct. 95, 142–153.
Thai, S., Thai, H.T., Vo, T.P., Patel, V.I., 2017. Size-dependant behaviour of functionally graded microplates based on the modified strain gradient elasticity theory and isogeometric analysis. Comput. Struct. 190, 219–241.
Torabi, J., Ansari, R., Darvizeh, M., 2018. A C^1 continuous hexahedral element for nonlinear vibration analysis of nano-plates with circular cutout based on 3D strain gradient theory. Compos. Struct. 205, 69–85.
Torabi, J., Ansari, R., Darvizeh, M., 2019. Application of a non-conforming tetrahedral element in the context of the three-dimensional strain gradient elasticity. Comput. Methods Appl. Mech. Eng. 344, 1124–1143.
Wang, B., Zhao, J., Zhou, S., 2010. A micro scale Timoshenko beam model based on strain gradient elasticity theory. Eur. J. Mech. Solid. 29 (4), 591–599.
Wang, B., Zhou, S., Zhao, J., Chen, X., 2011. A size-dependent Kirchhoff micro-plate model based on strain gradient elasticity theory. Eur. J. Mech. Solid. 30 (4), 517–524.
Yaghoubi, S.T., Balobanov, V., Mousavi, S.M., Niiranen, J., 2018. Variational formulations and isogeometric analysis for the dynamics of anisotropic gradient-elastic Euler-Bernoulli and shear-deformable beams. Eur. J. Mech. Solid. 69, 113–123.
Zeighampour, H., Beni, Y.T., Dehkordi, M.B., 2018. Wave propagation in viscoelastic thin cylindrical nanoshell resting on a visco-Pasternak foundation based on nonlocal strain gradient theory. Thin-Walled Struct. 122, 378–386.
Zervos, A., 2008. Finite elements for elasticity with microstructure and gradient elasticity. Int. J. Numer. Methods Eng. 73 (4), 564–595.
Zervos, A., Papanicolopulos, S.A., Vardoulakis, I., 2009. Two finite-element discretizations for gradient elasticity. J. Eng. Mech. 135 (3), 203–213.
Zhang, D.G., 2013. Nonlinear bending analysis of FGM elliptical plates resting on two-parameter elastic foundations. Appl. Math. Model. 37 (18–19), 8292–8309.
Zhang, G.Y., Gao, X.L., 2020. A new Bernoulli–Euler beam model based on a reformulated strain gradient elasticity theory. Math. Mech. Solid 25 (3), 630–643.
Zhang, B., He, Y., Liu, D., Shen, L., Lei, J., 2015. Free vibration analysis of four-unknown shear deformable functionally graded cylindrical microshells based on the strain gradient elasticity theory. Compos. Struct. 119, 578–597.